Selective Neuronal Vulnerability in Alzheimer's Disease: A Network-Based Analysis

Highlights

- Ribosomal profiling of AD vulnerable/resistant neurons in 5-, 12-, 24-month old mice

- Using human neuron-type functional networks and GWASs to model vulnerability

- Identification of axon plasticity genes linking Aß, aging, tau in vulnerable neurons

- PTB, regulator of tau exon 10 splicing, might contribute to selective vulnerability

Authors

Jean-Pierre Roussarie, Vicky Yao, Patricia Rodriguez-Rodriguez, ..., Marc Flajolet, Olga G. Troyanskaya, Paul Greengard

Correspondence

jroussarie@rockefeller.edu (J.-P.R.), ogt@cs.princeton.edu (O.G.T.)

In Brief

Neurons display different levels of vulnerability to Alzheimer's pathology. Roussarie et al. experimentally profile and computationally model several relevant neuron types. Using a mouse-human framework, they identify genes linking Aß, aging, and tau in vulnerable neurons. Finally, they show experimentally that PTB, a regulator of tau splicing, contributes to vulnerability.

Neuron

CellPress

NeuroResource

Selective Neuronal Vulnerability in Alzheimer's Disease: A Network-Based Analysis

Jean-Pierre Roussarie,[1,12,*] Vicky Yao,[2,3,4,12] Patricia Rodriguez-Rodriguez,[1,5] Rose Oughtred,[4] Jennifer Rust,[4] Zakary Plautz,[1] Shirin Kasturia,[1] Christian Albornoz,[1] Wei Wang,[1] Eric F. Schmidt,[6] Ruth Dannenfelser,[3,4] Alicja Tadych,[4] Lars Brichta,[1] Alona Barnea-Cramer,[1] Nathaniel Heintz,[6] Patrick R. Hof,[7] Myriam Heiman,[8,9,10] Kara Dolinski,[4] Marc Flajolet,[1] Olga G. Troyanskaya,[3,4,11,14,*] and Paul Greengard[1,13]

[1]Laboratory of Molecular and Cellular Neuroscience, The Rockefeller University, New York, NY 10065, USA
[2]Department of Computer Science, Rice University, Houston, TX 77005, USA
[3]Department of Computer Science, Princeton University, Princeton, NJ 08544, USA
[4]Lewis-Sigler Institute for Integrative Genomics, Princeton University, Princeton, NJ 08544, USA
[5]Department of Neurobiology, Care Sciences and Society, Division of Neurogeriatrics, Karolinska Institutet, 171 77 Solna, Sweden
[6]Laboratory of Molecular Biology, The Rockefeller University, New York, NY 10065, USA
[7]Nash Family Department of Neuroscience, Ronald M. Loeb Center for Alzheimer's Disease, and Friedman Brain Institute, Icahn School of Medicine at Mount Sinai, New York, NY 10029, USA
[8]Department of Brain and Cognitive Sciences, MIT, Cambridge, MA 02139, USA
[9]Picower Institute for Learning and Memory, Cambridge, MA 02139, USA
[10]Broad Institute of MIT and Harvard, Cambridge, MA 02142, USA
[11]Flatiron Institute, Simons Foundation, New York, NY 10010, USA
[12]These authors contributed equally
[13]Deceased April 13, 2019
[14]Lead Contact
*Correspondence: jroussarie@rockefeller.edu (J.-P.R.), ogt@cs.princeton.edu (O.G.T.)
https://doi.org/10.1016/j.neuron.2020.06.010

SUMMARY

A major obstacle to treating Alzheimer's disease (AD) is our lack of understanding of the molecular mechanisms underlying selective neuronal vulnerability, a key characteristic of the disease. Here, we present a framework integrating high-quality neuron-type-specific molecular profiles across the lifetime of the healthy mouse, which we generated using bacTRAP, with postmortem human functional genomics and quantitative genetics data. We demonstrate human-mouse conservation of cellular taxonomy at the molecular level for neurons vulnerable and resistant in AD, identify specific genes and pathways associated with AD neuropathology, and pinpoint a specific functional gene module underlying selective vulnerability, enriched in processes associated with axonal remodeling, and affected by amyloid accumulation and aging. We have made all cell-type-specific profiles and functional networks available at http://alz.princeton.edu. Overall, our study provides a molecular framework for understanding the complex interplay between Aβ, aging, and neurodegeneration within the most vulnerable neurons in AD.

INTRODUCTION

Selective neuronal vulnerability is a shared property of most neurodegenerative diseases (Saxena and Caroni, 2011). In the early stages of Alzheimer's disease (AD), the most common form of age-related dementia, clinical symptoms (such as memory loss) are caused by selective degeneration of principal neurons of the entorhinal cortex layer II (ECII), followed by CA1 pyramidal cells in the hippocampus and pyramidal neurons in neocortical association areas. In contrast, other brain regions, such as the primary sensory cortices, are relatively resistant to degeneration until later stages of the disease (Arnold et al.,

1991; Bussière et al., 2003; Fukutani et al., 2000; Gómez-Isla et al., 1996; Hof and Morrison, 1990; Hyman et al., 1984; Morrison and Hof, 1997; West et al., 1994). The molecular basis for this selective vulnerability remains unknown.

AD is characterized by two major pathological hallmarks: accumulation of the β-amyloid (Aβ) peptide (the main constituent of amyloid plaques) and formation of neurofibrillary tangles (NFTs; aggregates of hyperphosphorylated tau proteins that are thought to occur downstream of Aβ accumulation). Amyloid plaques do not accumulate in discrete brain areas. Rather, they are relatively widespread across most regions of the neocortex, followed by the entorhinal cortex and hippocampus, of AD

CellPress

patients (Sepulcre et al., 2017; Thal et al., 2002). In contrast, NFTs exhibit the same regional pattern as neurodegeneration (Braak and Braak, 1991; Bussière et al., 2003; Lewis et al., 1987). The co-occurrence of NFTs and neurodegeneration, as well as the fact that the best pathological correlate for clinical symptoms to date is the extent of NFT formation (Arriagada et al., 1992; Brier et al., 2016; Giannakopoulos et al., 2003), highlight the importance of tau pathology. Genetic analyses have revealed the central role of microglial cells and of their crosstalk with neurons in the disease (Efthymiou and Goate, 2017). Selective neuronal vulnerability could be due to intrinsic properties of vulnerable neurons or, alternatively, due to the surrounding microglia. However, recent evidence suggests that the regional particularities of microglia are primarily driven by differences in the neighboring neurons (Ayata et al., 2018), but the molecular drivers of the neuronal component of the pathological cascade that leads from Aβ accumulation to NFT formation and neurodegeneration are still largely unknown.

To understand and model cell-type-specific vulnerability in AD, we must gain insight into the molecular-level differences that predispose some neurons, before any pathological process becomes visible, to develop tau pathology earlier and faster than others. This requires high-quality cell-type-specific profiles of vulnerable and resistant neurons in healthy, non-diseased states. Although some neuron types of relevance to AD were profiled in a mouse hippocampal study (Cembrowski et al., 2016), the most vulnerable neuron type in early AD (ECII) has not been studied previously *ex vivo*. In humans, Small et al. (2005) profiled the whole entorhinal cortex (EC) and dentate gyrus (DG) in control and AD patients (Small et al., 2005), and the Allen Brain Atlas (ABA) provides a large dataset for a number of human brain regions (Hawrylycz et al., 2015), but neither of these studies is cell-type-specific. A comprehensive dataset of neuron-specific AD-relevant profiles has been generated by Liang et al. (2007). However, although valuable, human samples, including those in the studies cited above, are inevitably subject to degradation and postmortem changes and, in the context of AD, do not allow for direct probing of the effect of aging and Aβ accumulation on gene expression.

Furthermore, a key challenge in achieving a molecular understanding of selective neuronal vulnerability in AD is that vulnerability and pathology are likely not simply the result of a few genes or even pathways acting in isolation. Deciphering the pathological cascade requires cell-type-specific systems-level analyses and modeling of the complex molecular interactions that underpin the vulnerability of specific neurons to AD, going beyond differential gene expression and pathway enrichment analysis. Previous work examining whole-brain lysates from AD patients and non-demented individuals (Miller et al., 2008; Mostafavi et al., 2018; Zhang et al., 2013) demonstrated the promise of network analyses in AD, but these studies were limited to larger brain regions and, thus, could not address cell-type-specific vulnerability.

Here, we provide the first molecular framework to understand the interactions between age, Aβ, and tau within neurons. Our approach (Figure 1A) integrates the precision of cell-type-specific profiling across age in the non-diseased mouse with computational modeling of human neuronal omics (e.g., expression, interaction) data. Importantly, we show that the molecular

identity of AD-vulnerable and -resistant neurons is largely conserved between mouse and human, justifying use of the mouse to gain insight into selective neuronal vulnerability. All subsequent analyses use human data—including human network models for each neuron type and disease signals from human quantitative genetics data, ensuring relevance for AD neuropathology. The neuron-specific expression profiles and functional networks are available for download and exploration in an interactive web interface (http://alz.princeton.edu).

RESULTS

Cell-Type-Specific Profiling of Mouse Neurons with Differential Vulnerability to AD

To investigate the selective vulnerability of neurons in AD, we generated cell-type-specific expression profiles spanning the entirety of adulthood for vulnerable and resistant neurons using the bacTRAP (bacterial artificial chromosome—translating ribosome affinity purification) technology in wild-type mice (Doyle et al., 2008; Heiman et al., 2008). The bacTRAP technology enabled us to assay AD-relevant neuronal cell types with genome-wide coverage, measure transcripts *ex vivo* (as opposed to postmortem), and specifically capture actively translated (rather than all transcribed) genes.

We focused on the vulnerable principal neurons of ECII and pyramidal neurons of CA1 as well as five types of resistant neurons: pyramidal neurons of CA2, CA3, the primary visual cortex (V1), the primary somatosensory cortex (S1), and granule cells of the DG. Specifically, we constructed different transgenic mouse lines for each type of neuron, overexpressing the ribosomal protein L10a fused to enhanced green fluorescent protein (EGFP) under the transcriptional control of a driver specific to that type of neuron (Figure 1B). The bacTRAP procedure consists of immunoprecipitation of EGFP-tagged polysomes from EGFP-L10a-expressing cells, isolating actively translated neuron-specific mRNAs for RNA sequencing (RNA-seq). Previous work using bacTRAP or similar technologies (e.g., RiboTag) has demonstrated strong enrichment for cell-type-specific signal from cells expressing the tagged ribosomal protein (Brichta et al., 2015; Clarke et al., 2018; Doyle et al., 2008; Heiman et al., 2008; Sanz et al., 2009; Sun et al., 2015).

We first performed multidimensional scaling analysis of the resulting bacTRAP data and found that the samples (3–12 biological replicates per neuron type per age) clustered primarily by tissue location, as expected, with clear separation between the ECII, hippocampal regions (CA1, CA2, CA3, and DG), and neocortical regions (S1 and V1) (Figure 2A). We further verified the expression patterns of known neuron-type-specific markers (Figure 2B) and identified the top enriched genes for each neuron type in our data (Figure 2C; Table S1). Comparisons with the semiquantitative *in situ* hybridization (ISH) data in the ABA (Figure S1; STAR Methods) show that our data include the cell-type-specific signals in these datasets while providing substantially higher regional and quantitative genome-scale coverage. Thus, our approach provides a high-quality genome-wide assay of *ex vivo* neuron-type-specific expression in AD-vulnerable and AD-resistant regions of the brain. We provide an interactive web interface (http://alz.princeton.edu) to explore these expression data.
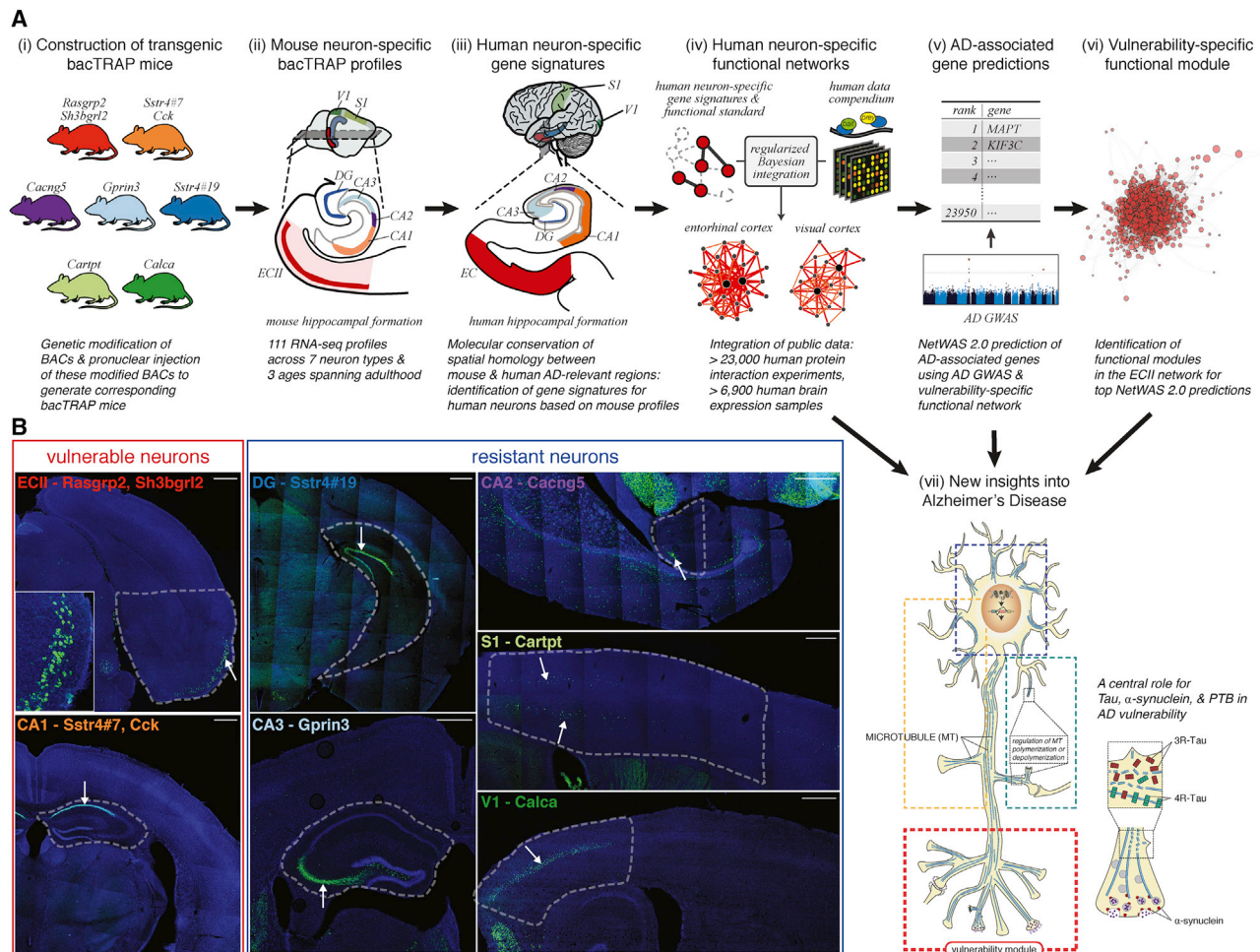
Figure 1. An Integrative Experimental Genomics and Bioinformatics Framework Combining Mouse and Human Data to Identify Genes and Pathways Involved in AD

(A) Overview of our framework. (i) To obtain molecular profiles of neurons that are vulnerable and neurons that are resistant to AD, we constructed bacTRAP mice for seven neuron types (see B). (ii) 111 neuron-specific high-quality *ex vivo* expression profiles were obtained for each neuron type at three different ages (5, 12, and 24 months), using bacTRAP followed by deep sequencing. bacTRAP allows fast isolation of actively translated RNA with minimal alterations of mRNA content after death of the animal and quantitative assessment of gene expression over a large range of expression levels. (iii) Using these data, we generated neuron-specific molecular signatures in mouse and human and created a spatial homology map between the two organisms. (iv) We used these neuron-specific signatures to construct seven neuron-specific functional networks through Bayesian integration of a compendium of more than 30,000 human experiments. (v) We identified genes functionally associated with AD pathology by combining the network for the most vulnerable neuron (ECII) with an AD tau pathology GWAS (Beecham et al., 2014) using our NetWAS 2.0 machine learning approach. (vi) These genes form distinct functional modules in the vulnerable neuron-specific network, with one module in particular capturing vulnerability-specific signals. (vii) Our analyses point to involvement of neurotransmitter release and axono-genesis in AD vulnerability as well as a central role of regulation of tau and α-synuclein by the RNA-binding protein PTB. Overall, we map AD-associated processes and their potential regulation by aging and Aβ in ECII neurons, providing the first molecular dissection of the AD pathological cascade within vulnerable neurons.

(B) bacTRAP transgenic mice generated for molecular profiling of vulnerable and resistant neurons. For each line, brain sections were stained with an anti-EGFP antibody (green) and counterstained with DAPI (blue). Genes whose regulatory regions we used for driving EGFP-L10a expression are indicated in each frame. For ECII and CA1, we show a section from the Rasgrp2- and the Sstr4#7-bacTRAP line, respectively, but also used the Sh3bgrl2- and Cck-bacTRAP lines for subsequent analyses. The dashed line delineates the brain region dissected out for bacTRAP. Arrows point to the neurons of interest, which overexpress EGFP-L10a. Scale bars, 500 μm.

ECII, principal neurons of the layer II of the entorhinal cortex; CA1, CA2, and CA3, pyramidal neurons of hippocampus CA1, CA2, and CA3, respectively; DG, granule neurons of the dentate gyrus; S1 and V1, pyramidal neurons of the primary somatosensory and visual cortex, respectively.

To characterize molecular signatures for AD-vulnerable cells in the non-disease state, we compared gene expression profiles of ECII and CA1 neurons against the five AD-resistant neuron types in wild-type mice (Table S1). Among the significantly enriched processes, we found many AD-relevant pathways (Figure 2D). Furthermore, one of the gene sets most enriched in vulnerable neurons was annotated AD-associated genes (Kyoto Encyclopedia of Genes and Genomes [KEGG] AD genes [hsa05010],
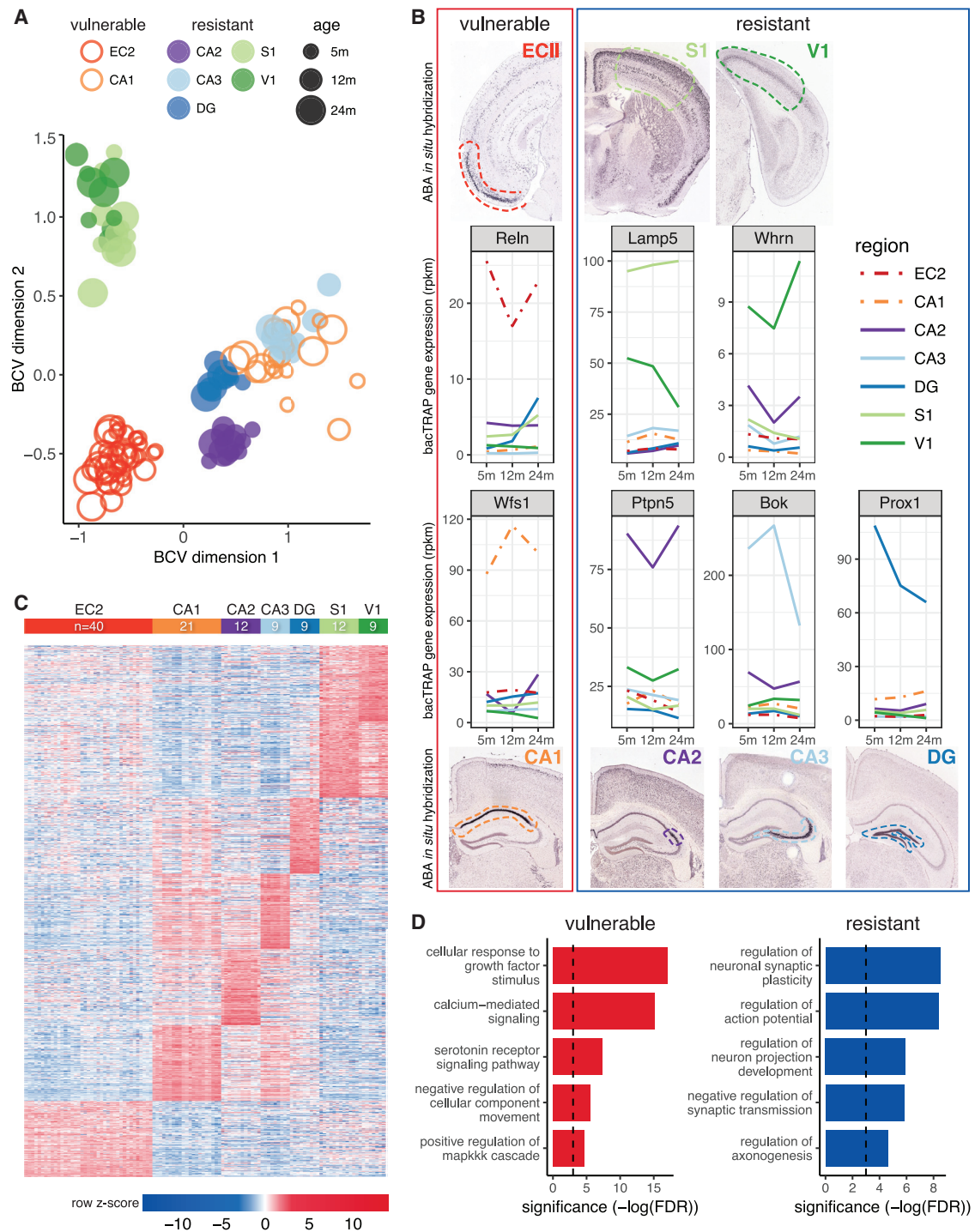
Figure 2. Molecular Characterization of Vulnerable and Resistant Neurons

(A) Multidimensional scaling analysis of all samples, demonstrating clustering of samples by region of origin. Each dot represents one sample (two mice pooled). Red (ECII) and orange (CA1) dots correspond to AD-vulnerable neurons. Purple (CA2), light blue (CA3), dark blue (DG), light green (S1), and dark green (V1) dots correspond to resistant neurons. Increasing dot sizes represent increasing mouse age (5, 12, and 24 months).

(B) Verification of our quantitative, neuron-specific RNA-seq profiles for known markers by ISH (ABA) (Lein et al., 2007). Shown is expression of previously described cell-type-specific markers across the seven types of neurons: Reln for ECII neurons (Pesold et al., 1998), Wfs1 for CA1 pyramidal neurons (Lein et al., 2004), Ptpn5 (or Step) for CA2 pyramidal neurons (Kohara et al., 2014), Bok for CA3 pyramidal neurons (Lein et al., 2004), Prox1 for DG granule neurons (Liu et al., 2000), Whrn for V1 layer IV (Dugas-Ford et al., 2012), and Lamp5 (or C20orf103) for S1 layers II and III (Zeng et al., 2012). For each marker, we show expression at

(legend continued on next page)

Neuron
NeuroResource

CellPress

one-sided Wilcoxon rank-sum test, $p < 9.41 \times 10^{-7}$). These results support the hypothesis that there are intrinsic differences between vulnerable and resistant neurons, present even in healthy individuals. We aim to leverage these differences in our framework to understand why the vulnerable neurons are preferential substrates for development of AD pathogenesis.

Neuron-Specific Spatial Homology between Mouse and Human

An important question for interpreting model organism studies of AD is whether the molecular identity of neurons is conserved between mouse and human. Previous comparisons using spatially resolved semiquantitative ISH (Zeng et al., 2012) or transcriptomics and proteomics without cellular resolution (Carlyle et al., 2017; Strand et al., 2007; Walker and Jucker, 2017) have suggested that mouse and human regional expression patterns are correlated, but the conservation of expression across neuronal subtypes requires further exploration.

In humans, fully quantitative data at cell-type-specific resolution is lacking across the regions most relevant for AD. However, the discrete brain structure microarray data from the ABA (Hawrylycz et al., 2015) captures enough regional specificity for an expression-based comparison between the seven mouse neuronal subtypes and 205 human brain regions. We calculated a spatial homology score between molecular signatures for each mouse neuron type and each human brain region, generating 1,435 pairwise spatial homology measurements. Remarkably, of all these possible mappings, we found a nearly perfect match between each mouse profile and its corresponding relevant human brain region (Figure 3; Table S2; Figure S2A; $p < 0.0001$, permutation test, n = 10,000). This confirms the validity of leveraging the power of *ex vivo* neuron-specific molecular profiles in the mouse to gain relevant insight into the molecular characteristics of the most vulnerable neurons in human AD. Although there are differences in lifespan and other factors relevant to AD that may facilitate the degeneration of human neurons (Walker and Jucker, 2017), our comparison supports the notion that physiological differences between vulnerable and resistant neurons are conserved. This study provides, to our knowledge, the first systematic evidence that the molecular identity of AD-relevant neuron types is conserved between the mouse and human brain. This supports our approach of combining the cell-type-specific signals in healthy mouse neurons with AD-relevant signals in large collections of human data.

In Silico Modeling of Gene Networks in AD-Relevant Neuronal Cell Types

AD neurodegeneration is the result of multiple molecular-level changes to the system of interacting genes and pathways within vulnerable neurons. We model this system with cell-type-specific functional networks, i.e., maps of functional relationships between proteins in the specific cellular contexts of the different types of neurons. Specifically, a functional relationship represents the common involvement of two proteins, directly or indirectly, in a biological pathway in the cell type of interest. We recently developed a regularized Bayesian network integration method to construct tissue-specific functional networks (Greene et al., 2015). These network-level models are an effective first approximation of the functional landscape of a cell and have been successfully applied to the study of diseases (Greene et al., 2015; Krishnan et al., 2016; Song et al., 2016). It was, however, previously impossible to apply this method to construct networks at neuron-specific resolution because of limitations in high-quality cell-type-specific gene expression annotations in humans. Given the strong concordance between our mouse neuron-specific molecular signatures and their corresponding human brain regions, we used these signatures as positive examples to extract cell-specific signals from a large human data compendium including thousands of gene expression, protein-protein interaction, and shared regulatory profile datasets to construct human neuron-type-specific functional networks. We have made the resulting seven *in silico* human genome-wide network models, each representing one AD-vulnerable or -resistant neuron type in the non-disease state, available for download and dynamic, query-based exploration at http://alz.princeton.edu.

To identify functional characteristics and differences specific to neuron types vulnerable or resistant to AD, we examined the functional cohesiveness of biological processes (i.e., a measure of network connectivity among genes known to be part of that process) in each corresponding functional network model (Table S1). We found that pathways neuroprotective in AD (Caraci et al., 2008; Liu et al., 2014; Tesseur et al., 2006) appeared to be more cohesive in AD-resistant neurons than in vulnerable neurons; namely, the transforming growth factor β receptor signaling pathway (in the DG) and the canonical Wnt signaling pathway (in the DG, S1, and V1). On the other hand, mitochondrial processes like apoptotic mitochondrial changes and mitochondrial fission were more cohesive in CA1 and ECII, respectively, which is consistent with the saliency of mitochondrial dysfunction at early stages of the disease (Du et al., 2010). Strikingly, we found that the processes with the largest functional cohesiveness in vulnerable compared with resistant neurons were all related to microtubule organization. This is the first evidence that these tau-regulated processes may intrinsically differ between vulnerable and resistant neurons in the healthy, non-diseased state.

Identifying AD-Associated Genes through Integration of AD GWASs and the ECII Functional Network

To identify potential genes involved in AD neuropathology, we then combined these network models of vulnerable neuron function with unbiased disease signals from human quantitative

5, 12, and 24 months of age. Each color represents a different type of neuron. We also show, for each gene, an ISH image from the ABA that shows expression in the corresponding neurons. Image credit: Allen Institute.

(C) Heatmap of gene expression for the top 500 genes enriched in each neuron type. For each gene (rows, grouped by neuron type in which they are enriched) and sample (columns, grouped by cell type, including all three different ages), the row-normalized $\log_2(RPKM)$, where RPKM stands for reads per kilobase million, is displayed, showing that hundreds of genes are enriched in each type of neuron.

(D) Pathways enriched in vulnerable (red) and resistant (blue) neurons, with their significance [$-\log(FDR)$] of enrichment.
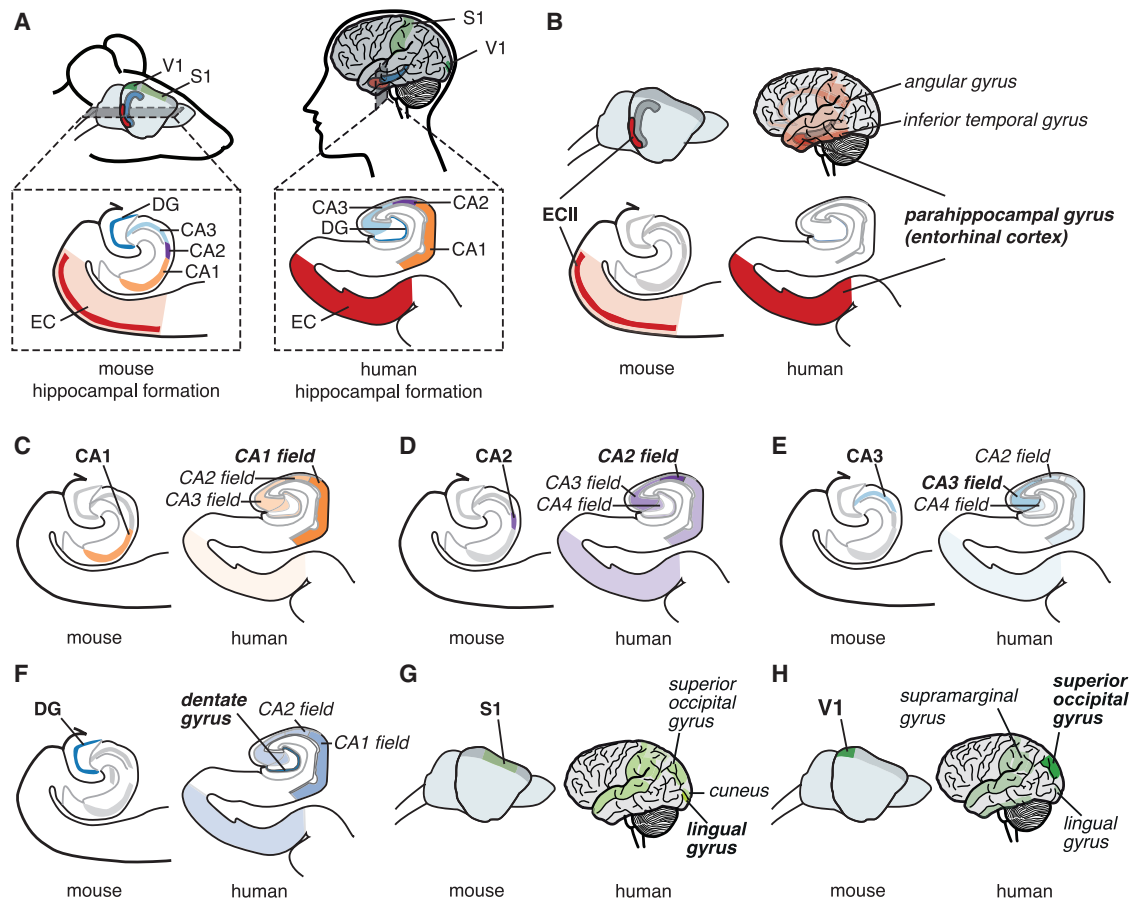
See also Table S1 and Figure S1.

Figure 3. Conservation of Molecular Identity of Seven AD-Vulnerable and -Resistant Neuronal Types between Mouse and Human
(A) Location in the mouse and human brain of the seven brain regions included in this study (lateral view of the whole brain and close-up of the hippocampal formation). To validate the use of mouse profiles for study of the human disease, we compared the molecular signatures of mouse neurons derived from 111 mouse bacTRAP samples with 205 human brain region-specific expression profiles from the Allen Institute.
(B–H) For each mouse neuron type (B, ECII; C, CA1; D, CA2; E, CA3; F, DG; G, S1; H, V1), the human brain regions with molecular signatures closest to each mouse neuron type are highlighted (the more opaque the color of a brain region, the higher the similarity with the mouse neuron type). Note that we find a nearly perfect correspondence between mouse neurons and human brain regions.
See also Table S2 and Figure S2A.

genetics data. Specifically, we developed an approach, Network-Wide Association Study 2.0 (NetWAS 2.0), that extends our previously described (Greene et al., 2015) framework with a probabilistic subsampling method to take into account gene-level confidence from quantitative genetics studies. This machine learning approach leverages genome-wide association studies (GWASs) in conjunction with a functional network specific to the region of interest to identify cell-type-specific network patterns predictive of a disease, reranking all genes based on disease relevance significantly better than the original GWAS (Greene et al., 2015).

Because many cortical neurons eventually develop pathology at late stages of AD, we expect to find disease-relevant signals with all network models, with the network model for the most vulnerable neuron type capturing the bulk of vulnerability signals. To specifically focus on neuronal genes leading to degeneration as opposed to the varied other disease components that eventually lead to cognitive decline, we used a neuropathologically

rather than clinically defined AD GWAS; namely, a GWAS for Braak stage (NFT pathology-based staging; Beecham et al., 2014). We applied NetWAS 2.0 by using the network model for the most vulnerable neurons (ECII) to reprioritize genes based on this Braak-stage GWAS (Table S3). Remarkably, MAPT (microtubule-associated protein tau, the gene that encodes tau, the primary component of NFTs) was ranked first among all 23,950 reprioritized genes. In spite of previous genetic evidence for association between tau and AD (a rare variant of tau has been shown to increase AD risk [Coppola et al., 2012] as well as neuronal vulnerability [Silva et al., 2016], and a tau haplotype was associated with EC atrophy [Desikan et al., 2015]), MAPT was not nominally significant in the initial GWAS (initial GWAS tau p = 0.269). This illustrates the power of NetWAS 2.0 to extract important disease-relevant signals that may be hidden in the original GWAS. The identification of genes associated with tau pathology using the Braak-stage GWAS was further corroborated by significantly overlapping results

Neuron
NeuroResource

CellPress

obtained by applying NetWAS 2.0 to two recent independent neuropathologically associated AD GWASs (one-sided Fisher's exact test comparing overlap of the top 10% genes: NFT-GWAS-based NetWAS, $p < 2.2 \times 10^{-16}$; cerebrospinal fluid pTau-GWAS-based NetWAS, $p < 2.2 \times 10^{-16}$) (Chibnik et al., 2018; Deming et al., 2017).

Overall, although the original GWAS for Braak stages was somewhat enriched for known AD-annotated genes (KEGG AD genes, one-sided Wilcoxon rank-sum test, $p < 0.199$), the reprioritized gene ranking was much more significantly enriched for these genes (one-sided Wilcoxon rank sum test, $p < 4.55 \times 10^{-8}$). We also observed strong enrichment of genes involved in regulation of Aβ accumulation and NFT formation (one-sided Wilcoxon rank-sum test, amyloid: $p < 1.29 \times 10^{-10}$, NFT-1: $p < 2.2 \times 10^{-16}$, NFT-2: $p < 2.2 \times 10^{-16}$, respectively, for gene sets curated by curators independent of the analyses; Table S4; Figures 4A and 4B). Known AD neuroprotective pathways, like the neurotrophin signaling pathway (Nagahara et al., 2009) and Wnt signaling pathway (Liu et al., 2014; Tesseur et al., 2006) were also predicted to be strongly associated (Table S3). Last, we highlight the association of neurotransmitter secretion with AD (false discovery rate [FDR] $< 2.57 \times 10^{-24}$). Dysregulation of this pathway is one of the most prominent effects of Aβ accumulation (Abromov et al., 2009), and the resulting hippocampal network hyperactivity was suggested to be a crucial contributor to AD pathogenesis (Bakker et al., 2012; Palop and Mucke, 2010; Vossel et al., 2013). Because the AD signal in NetWAS 2.0 comes only from unbiased GWAS data (i.e., no prior AD disease knowledge was incorporated), the NetWAS 2.0 results provide data-driven, unbiased prioritization of AD-associated processes of the many pathways that, over time, have been associated with tau pathology.

Beyond these well-characterized associations, one of the most significantly enriched pathways in the NetWAS 2.0 results was a microtubule-related process: regulation of microtubule cytoskeleton organization (FDR $< 1.38 \times 10^{-27}$; Table S3). This is consistent with our connectivity analysis, where we discovered that microtubule-regulating pathways were particularly cohesive in vulnerable neurons. Together, these results support the hypothesis that microtubule-regulating pathway genes may cooperate with MAPT for formation of NFTs in vulnerable neurons. Our data also strongly support a role of mRNA splicing and transport in AD pathogenesis (RNA splicing, FDR = 4.48×10^{-10}; RNA transport, FDR = 3.32×10^{-16}). RNA binding proteins in these processes have recently emerged as major players in various non-AD neurodegenerative diseases (Ramaswami et al., 2013), and recent studies have suggested possible involvement in AD—TIA1 protects against tau-mediated degeneration (Apicco et al., 2018), CELF1 is one of the main GWAS hits (Lambert et al., 2013), and the activity of ELAVL proteins is altered in AD brains (Scheckel et al., 2016).

Association of NetWAS 2.0 Genes with AD Pathology

We next investigated the link between key drivers of the AD pathological cascade (Aβ accumulation and age) and AD vulnerability-associated genes identified by NetWAS 2.0 analysis. Recall that we leveraged a tau pathology-based GWAS (Beecham et al., 2014) for the NetWAS 2.0 predictions, prioritizing genes that may modulate NFT formation. To enable direct analysis of the ECII-specific effects of Aβ accumulation in AD, we crossed our ECII bacTRAP mice with an AD mouse model (APP/PS1 mice). These mice overexpress mutant amyloid precursor protein (APP) and presenilin 1 (PSEN1) and have increased levels of Aβ in the cortex and hippocampus (Borchelt et al., 1997). We profiled ECII neurons at 6 months of age, when the first plaques start to form (Table S4). Genes significantly downregulated in APP/PS1 mice were strongly enriched in our top NetWAS 2.0 gene predictions (one-sided Wilcoxon rank-sum test, $p < 9.21 \times 10^{-14}$). Additionally, genes modified by aging in ECII of wild-type mice (24- versus 5-month-old mice; Table S4) were also strongly enriched at the top of our ranking (one-sided Wilcoxon rank-sum test, $p < 4.19 \times 10^{-13}$). Our finding that Aβ and aging modulate the expression of genes predicted by NetWAS 2.0 to be associated with tau pathology indicates that these genes might connect Aβ accumulation and NFT formation in the age-dependent AD pathological cascade.

To directly examine the possible relationship between top NetWAS 2.0 genes and human AD pathology, we used data from two independent human datasets. The Adult Changes in Thought (ACT) study (Miller et al., 2017) provides paired gene expression data and pathology measurements from hippocampus samples of elderly individuals at risk for dementia. For each gene, we calculated the correlation between expression level and the amount of amyloid plaques. We found that expression of our top gene predictions was significantly more correlated with amyloid burden than background or genes implicated in the original Braak-stage GWAS (bootstrap $p < 0.0001$; Figure 4C). Top NetWAS 2.0 predictions obtained using the ECII functional networks were also more significantly correlated with amyloid plaque amount than top predictions obtained using the functional networks for resistant neurons (Figure S2B). Furthermore, our predictions were very significantly enriched in genes differentially downregulated in ECII neurons of sporadic AD patients measured in a different study (relative to control patients, one-sided Wilcoxon rank-sum test, $p < 2.2 \times 10^{-16}$) (Liang et al., 2008). This consensus of results indicates that the top NetWAS 2.0 gene predictions highlight genes that participate in the AD pathological cascade within neurons.

Identification of AD-Associated Functional Modules

To better understand the processes and pathways through which these genes are associated with NFT formation and AD, we clustered the genes with top NetWAS 2.0 ranks into functional modules within the ECII network (Figure 4D; Table S5) using a shared-nearest-neighbor-based community-finding algorithm (Blondel et al., 2008). We identified four modules, each enriched in distinct AD-associated processes, including RNA splicing (module A), metabolism (module B), neurotransmitter release (module C), and neuron differentiation (module D). Interestingly, several pathways were shared across multiple modules, including microtubule organization (modules A, C, and D) and axonogenesis (modules B, C, and D), supporting a central role of these processes in AD pathogenesis (Table S5).

We then further characterized these functional modules by examining their relationship to aging as well as Aβ accumulation and NFT formation in vulnerable neurons (Table S5). We found
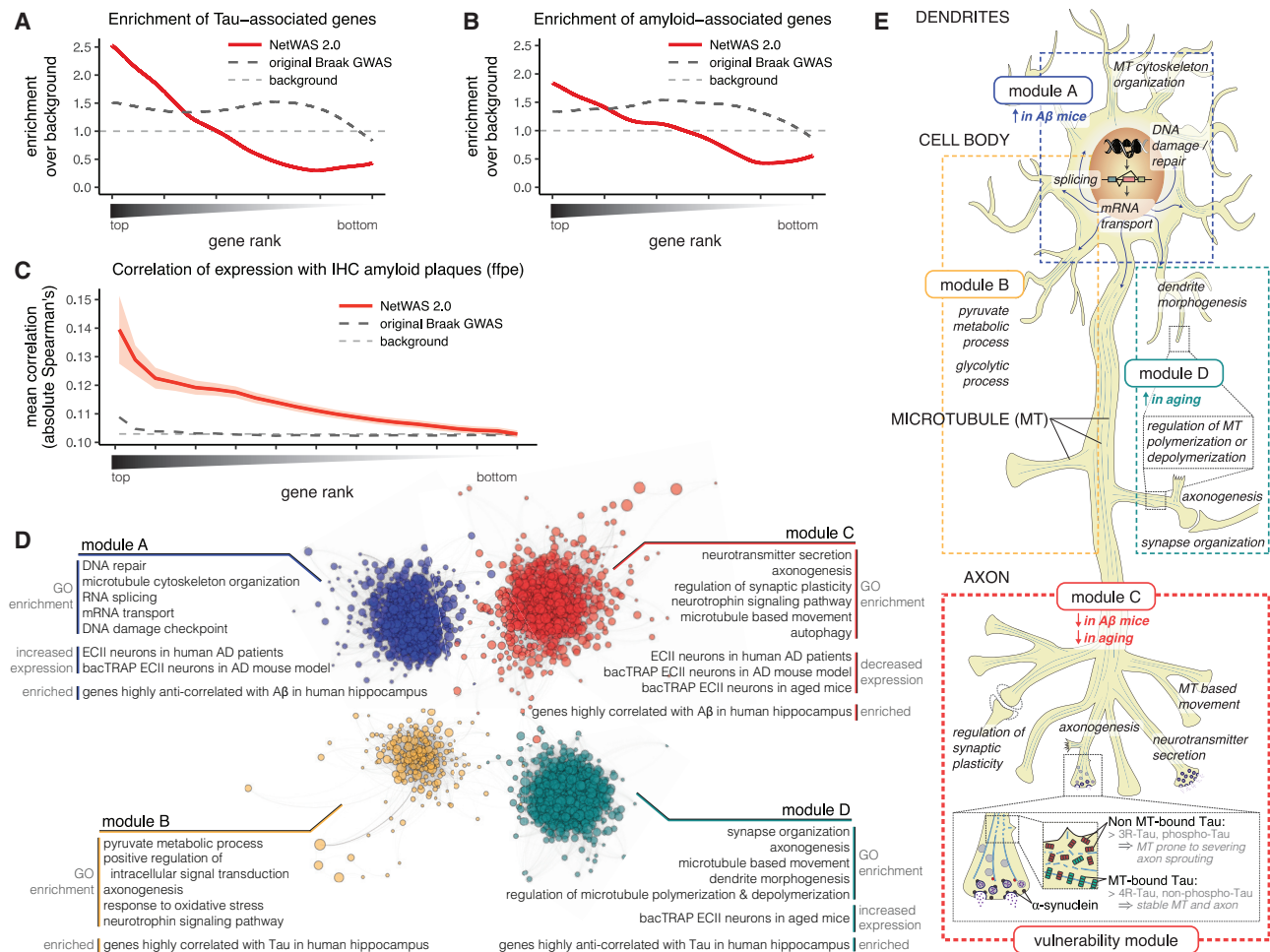
Figure 4. Prediction, Validation, and Functional Analysis of Genes Associated with AD Pathology

(A and B) Top NetWAS 2.0 gene predictions show significantly higher enrichment of NFT-associated (A) and Aβ-associated genes (B) (curated by an independent expert; Table S4) than the original GWAS used as input to NetWAS 2.0.

(C) Human hippocampus expression levels of top AD-associated gene predictions are highly correlated with amyloid plaque amounts in the ACT cohort (Miller et al., 2017). The x axis represents the proportion of top NetWAS 2.0 genes obtained. The average absolute values of correlations between gene expression level and amyloid plaques across the subset of genes are plotted (NetWAS 2.0 predictions in red with 95% confidence interval, Braak GWAS in black, background genes in gray).

(D) Clustering of the top 10% NetWAS 2.0 genes using a shared-nearest-neighbor-based community-finding algorithm identifies functional modules corresponding to distinct AD-associated processes. We indicate pathways enriched in each module as well as the association of each module with aging and AD pathology in our data (independent of our functional network analysis) and external datasets. Each dot represents a gene (where size inversely correlates with the NetWAS 2.0 ranking, i.e., larger dots represent top-ranked genes). Network layout (ForceAtlas) by gephi (Bastian et al., 2009) of ECII-specific network posterior probabilities above prior are shown (comembership score ≥ 0.75 based on 1,000 subsamples for visual clarity).

(E) Representation of pathways enriched in each module (D) in ECII neurons. Microtubules (MTs) are represented in blue. Enrichment for genes modulated by Aβ and aging is indicated for each module. Module A is enriched in neuronal cell body processes, whereas module C includes many axonal processes. Modules A, B, and D may be generally associated with tau pathology in many types of projection neurons, whereas module C might capture the surplus of vulnerability from ECII neurons. The module includes structural and functional axonal remodeling pathways, suggesting that axonal plasticity is key to the degeneration process in AD. Concomitant actions of Aβ and aging on module C genes might perturb crosstalk between axon remodeling processes and eventually impinge on SNCA and MAPT function. Magnified view of an axon terminal is inset. α-Synuclein, a regulator of neurotransmitter release, binds to synaptic vesicles (gray circles), to the membrane of the presynaptic active zone, and to MTs. Both forms of tau (3R in red and 4R in green) are present along MTs in axons, with 4R (as well as non-phosphorylated tau) having higher affinity for MTs than 3R (as well as hyperphosphorylated tau). Tau-bound MTs are less stable and more prone to severing, a requirement for axon sprouting and axonal plasticity. PTBP1 regulates tau isoform use and α-synuclein levels.

See also Tables S3–S6 and Figure S2B.

that neurotransmitter secretion-related module C genes showed decreased expression in the context of Aβ accumulation in the mouse (our APP/PS1 mouse profiling) and have significantly lower expression in aged wild-type mice. Thus, module C is a good candidate for linking Aβ accumulation with aging in the AD pathological cascade. Furthermore, module C was the only

module with ECII-specific signal for tau pathology (i.e., significantly enriched in genes downregulated in ECII neurons of AD patients but not strongly correlated with tau in non-ECII regions of the human hippocampal formation [ACT study]; Miller et al., 2017). Additionally, only module C demonstrated significantly tighter cohesiveness in ECII versus resistant neurons (Student's t test, intersection-union test, p < 0.0135). Thus, although modules A, B, and D may represent pathways common to general AD progression in any neuron type, module C may confer the surplus of susceptibility specific to ECII neurons. Because this vulnerability-specific module represents processes related to axon structural remodeling and presynaptic excitability, it is tempting to speculate that specific AD vulnerability of ECII neurons may be linked to their lifelong maintenance of a state of high axonal plasticity (Figure 4E).

Functional Association of α-Synuclein, tau, and PTB in ECII Neurons

To identify genes in this vulnerability-specific module that underlie ECII susceptibility in early-stage AD, we examined the connectivity and centrality of the module members across all seven neuron-specific networks. Intuitively, two genes are tightly connected in a specific neuronal context when they have a high-confidence link in the functional network for that neuronal type; this suggests involvement of these genes in shared processes. A highly central gene is one that has many high confidence links with other genes across the network, indicating involvement of this gene in a wide array of processes. Within module C, MAPT (tau) was the most centrally connected of all 668 module C genes in the ECII network, and our analysis pointed to SNCA (the gene encoding α-synuclein) as potentially driving the ECII specificity of this vulnerability-specific module. This is based on the finding that MAPT and SNCA are not only tightly connected to each other in the ECII network, but α-synuclein also has the highest differential network centrality between ECII and the resistant neurons (Table S6). This suggests that α-synuclein is associated with many more processes in ECII neurons than in other types of neurons, that tau cooperates with α-synuclein in many of these processes, and that α-synuclein may contribute to NFT formation upon dysregulation of these processes. This association between MAPT and SNCA in the context of AD neuronal vulnerability is supported by previous work demonstrating physical as well as functional interaction between these two proteins in other neurodegenerative disorders (reviewed in Moussaud et al., 2014). For example, tau and α-synuclein have been described previously to influence each other's aggregation into pathological lesions in Parkinson's disease as well as in mice overexpressing these genes (Emmer et al., 2011; Giasson et al., 2003; Khandelwal et al., 2010, 2012). However, a role of endogenous α-synuclein in formation of NFT has not been described previously, although a large proportion of AD patients present α-synuclein pathology (Hamilton, 2000).

PTB (NCBI GeneID: 5725), a regulator of alternative splicing (Llorian et al., 2010), was the protein most highly connected to α-synuclein and tau in the ECII network. It has not been linked previously to adult neural function; in fact, it has often been thought to be expressed predominantly during development and to be downregulated in the adult (Boutz et al., 2007; Zheng

et al., 2012). PTB has not been associated previously with AD, although a mini gene screen in cancer cell lines identified it as capable of regulating the splicing of tau exon 10 (Wang et al., 2004). Here, we found that PTB was actively translated in all adult mouse neurons profiled, and we detected significant amounts of the protein by western blot on adult mouse EC lysates (Figure S3A). Furthermore, we analyzed transcriptomics data from laser capture microdissected ECII neurons in humans (Liang et al., 2008) and from diverse brain regions in GTEx (GTEx Consortium) and found adult PTB expression in both (Figure S3B). In examining publicly available AD expression datasets, we found that, in AD compared with control patients, PTB is specifically upregulated in the parahippocampal gyrus, where the EC is located (Figure S3C; log fold change [logFC] = 0.22, p = 0.0004; Accelerating Medicines Partnership Alzheimer's disease project [AMP-AD], https://agora.ampadportal.org/genes). We also found significant upregulation of PTB in laser capture microdissected ECII neurons of AD patients (logFC = 0.39, p = 0.00099, AD versus control, GSE5281) (Dunckley et al., 2006).

We tested experimentally whether PTB can regulate SNCA and MAPT mRNA by measuring gene expression and differential exon use by RNA-seq after PTB knockdown in human neuroblastoma cells in vitro. Silencing PTB increased total SNCA levels and inclusion of MAPT exon 10, whereas there was no effect on any other MAPT exon (Figure 5A); we confirmed these results using quantitative PCR (Figures 5B and 5C; Figure S3D). Regulation of exon 10 is of high relevance for tau pathology because its inclusion gives rise to four- rather than three-microtubule binding repeat tau (4R- and 3R-tau, respectively). An imbalance between 4R- and 3R-tau has been shown repeatedly to give rise to tau pathology in different tauopathies as well as in AD (reviewed in Liu and Gong, 2008).

To directly investigate the effect of PTB on tau splicing in ECII neurons in vivo, we modulated PTB levels in the mouse EC by stereotaxically injecting recombinant adeno-associated viruses (AAVs). Here we overexpressed PTB because significant silencing of PTB in vivo could not be achieved in the mouse EC (Figures 5D and 5F; Figures S3E–S3H), likely because of the multiple mechanisms tightly regulating endogenous PTB expression (Wollerton et al., 2004; Yeom et al., 2018). We found that PTB overexpression affected exon use of a number of genes involved in microtubule dynamics or microtubule-based transport (e.g., Cdc42, Clip1, Dnm1, Eml4, Klc1, and Kif1b), supporting our earlier findings regarding the saliency of microtubule-related processes in vulnerable neurons (Figure S4).

Crucially, we discovered that PTB had a significant effect on human exon 10 use in transgenic mice expressing the full human wild-type tau gene (human tau phage artificial chromosome [htau PAC] mice) (Andorfer et al., 2003). Specifically, overexpression of PTB increased the 3R/4R ratio for human tau, as measured by fluorescence RT-PCR experiments using primers surrounding exon 10 (Figures 5E and 5G; Figure S3I; one-tailed paired Student's t test, p = 0.012), consistent with the decreased 3R/4R ratio observed when we silenced PTB in vitro. We further validated these results using quantitative PCR on total EC RNA (Figure S3J; one-tailed paired Student's t test, p = 0.012). Importantly, NFTs in ECII neurons have been shown to have
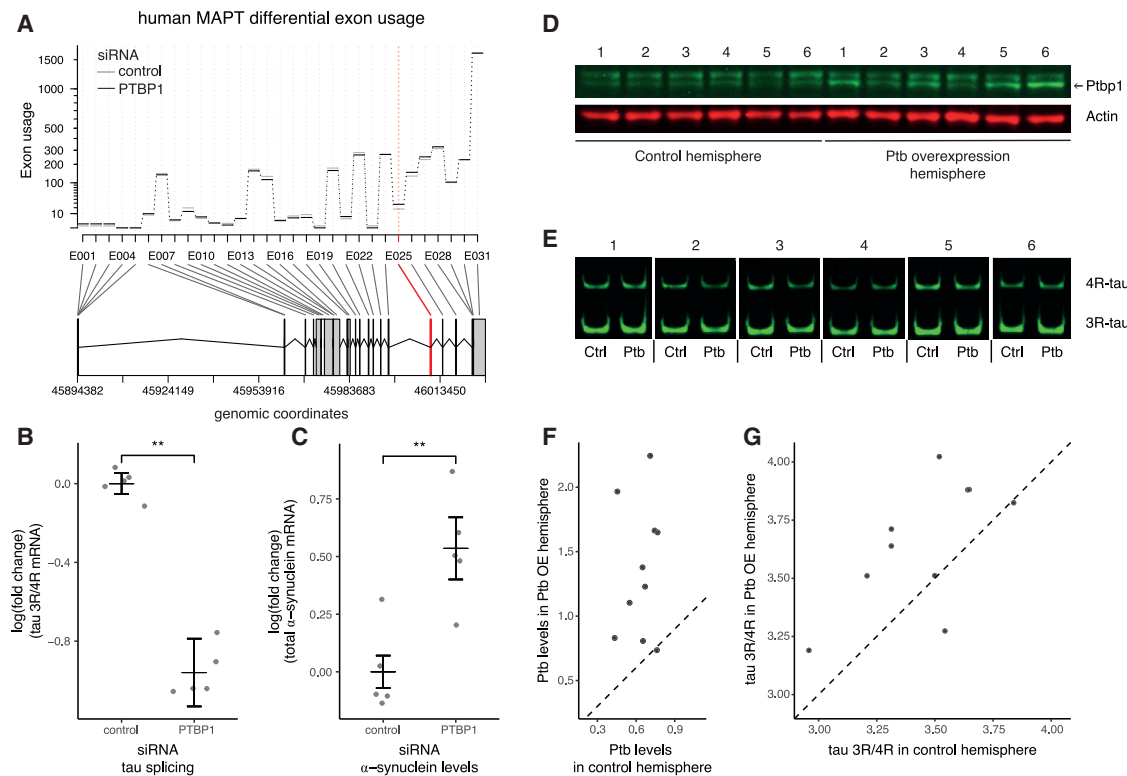
Figure 5. Modulation of MAPT Splicing and SNCA Levels by PTB

(A–C) Silencing of PTB in SH-SY5Y neuroblastoma cells. mRNA was purified after 3 days, and we analyzed mRNA by RNA-seq.

(A) DEXSeq (Anders et al., 2012) analysis showing which exonic parts of MAPT are changed. Only exon 10 is significantly changed (DEXSeq-adjusted p = 0.028).

(B) qPCR measurement of the 3R/4R tau ratio. The proportion of 3R tau decreases significantly, showing that PTB promotes exon 10 exclusion (Student's t test, p < 0.002). Error bars show standard error of the mean.

(C) qPCR measurement of SNCA levels. α-Synuclein is increased significantly (Student's t test, p < 0.006). Error bars show standard error of the mean.

(D–G) Overexpression of Ptb in the EC of htau PAC mice, which transgenically overexpress the entire wild-type human tau gene. Empty AAV1 particles or particles containing a cDNA for mouse Ptb (Δexon 9, the predominant isoform in adult neurons) were injected stereotaxically into the EC on opposite sides of the brain. qPCR and western blots were run on bulk lysates of the EC 1 week after injection. Ptb overexpression and control sides were paired.

(D) Western blot detection of Ptb in the EC *in vivo*. Numbers over the gel pictures represent individual mice.

(E) Fluorescence PCR assay to test differential use of human tau exon 10 on reverse-transcribed RNA from EC lysates. 3R-tau and 4R-tau in the lysate yield amplicons of different lengths. Numbers over the gel pictures represent individual mice.

(F) Quantification of Ptb protein overexpression in the EC on the Ptb OE (overexpression) side compared with the control side by quantitative western blot as in (D) (two experiments, n = 10 mice total, paired one-tail Student's t test, p = 8.3 × 10^{-4}).

(G) Quantification of human tau exon 10 splicing using fluorescent PCR as in (E) on EC lysates of injected mice. There is a significant decrease in human exon 10 use (increase in human 3R-tau) upon Ptbp1 overexpression (two experiments, n = 10 mice total, paired one-tailed Student's t test = 0.012). Of note, tau splicing is measured on bulk lysates of EC, potentially yielding a modest effect because of ECII-specific signal dilution.

See also Figures S3 and S4.

significantly larger 3R/4R tau ratios than NFTs in other hippocampal neurons (Hara et al., 2013; Iseki et al., 2006). This regional imbalance, previously unexplained, could contribute to the preferential NFT deposition in ECII neurons. ECII-specific dysregulation of PTB could thus be one of the driving factors for early initiation of tau pathology in these neurons, potentially contributing to their vulnerability.

DISCUSSION

Little is known about the molecular basis of selective neuronal vulnerability in AD and the molecular pathways that lead to NFT formation and neurodegeneration. Furthermore, no animal model comprehensively recapitulates every aspect of human

AD pathogenesis. Although the templated spread of tau along axonal routes (Kaufman et al., 2018) could explain the chronology of NFT appearance later in the disease, pathological tau can only form *ex nihilo* in the most vulnerable neurons because of the intrinsic properties of these neurons. Kaufman et al. (2018) recently showed that EC isolates from AD patients were the first to gain tau seeding potential, before isolates from any other region of the brain, further demonstrating that pathology is not passed on to EC from another region. A molecular dissection of the initial step whereby tau pathology forms in the EC has long remained elusive.

Here we provide an integrative and unbiased framework for the study of AD that combines the advantages of mouse models and human data. Our approach (1) models AD-vulnerable and

Neuron
NeuroResource

CellPress

-resistant human neurons *in silico* with high-quality cell-type-specific molecular profiles generated in the non-diseased mouse and a compendium of publicly available human data, (2) leverages human quantitative genetics to identify genes and pathways relevant for AD pathology within these *in silico* models, and (3) experimentally tests, in the mouse, the effect of age and Aβ, a major AD endophenotype, on the genes we predict to be associated with AD pathology, elucidating the pathological cascade of AD. Our approach is general and applicable to any complex disease with selective cell vulnerability where relevant human GWAS data are available. For neurodegenerative diseases with a complex multicellular pathogenesis, the approach also allows identification of cell-type-specific pathological pathways.

Previous network-based approaches (Miller et al., 2008, 2013; Mostafavi et al., 2018; Zhang et al., 2013) were successful attempts to leverage functional genomics for molecular dissection of AD. Their use of bulk genomics data allowed them to study gene expression patterns from all cell types, but also limited their ability to precisely identify neuronal processes. Our framework focused on leveraging neuron-type-specific network models and enabled us to further pinpoint an axon plasticity module responsible for the vulnerability of ECII neurons. Furthermore, use of a rich array of functional genomics data for construction of the networks allowed us to identify interactions between genes that are not purely based on coexpression, including modulation of tau splicing by PTB. Our study is also the first one to show the centrality of the tau and α-synuclein genes in the disease process within vulnerable neurons, although these genes are not enriched in vulnerable neurons.

Using this approach, we identify molecular mechanisms underlying neuronal vulnerability in AD. In addition to significantly predicting many of the genes associated previously with AD, we also outline novel pathways linking Aβ and tau pathology. Of the numerous genes revealed by our framework, one of the most striking ones is PTB, a splice factor dysregulated in AD, which, as we show, modulates the 3R/4R-tau balance. An excess of 3R-tau is thought to be the cause of a number of familial frontotemporal dementia cases (Liu and Gong, 2008). In other tauopathies, like corticobasal syndrome, NFTs are exclusively constituted of 4R-tau (Liu and Gong, 2008). Deviation from the physiological 3R/4R equimolar balance is thus considered to contribute to tau aggregation. In AD, vulnerable-neuron-specific dysregulation of PTB could precipitate a 3R/4R imbalance in these neurons and explain their premature accumulation of NFTs.

More generally, our unbiased data-driven analyses place microtubule dynamics at the center of AD pathogenesis. We find that this process is one of the most salient characteristics of the most vulnerable neuronal subtype and closely associated with NFT formation. As key regulators of neuronal architecture and intraneuronal trafficking, microtubules are the endpoint of many neuronal processes. Thus, it is important to determine which specific pathways lead to dysregulation of microtubule dynamics in the context of AD. Although a conclusive answer to this question requires further study, our analyses of ECII vulnerability highlight two potential candidate processes: axonogenesis and synaptic vesicle release. Both have been linked previously to microtubule remodeling (Bodaleo and Gonzalez-Billault, 2016; Lewis et al.,

2013) and are connected to microtubule genes within the vulnerability-specific module. Interactions between structural and electrophysiological properties of the axon could be more prominent in ECII neurons (known to display considerable axon arborization; Tamamaki and Nojyo, 1993) than in other cell types, which could confer exceptional axonal plasticity to ECII neurons but could also be responsible for ECII vulnerability.

Successful therapeutic strategies for treating AD will likely involve diverse approaches. These might include molecular interventions that prevent neuronal pathology and eventual degeneration or acting on the glial response that accompanies the neuropathology and contributes to the clinical symptoms (microglia and astrocytes) or on the psychological and lifestyle interventions that can mitigate the symptoms. In any case, it is indispensable to gain an understanding of how the neuropathology begins and, in particular, how NFTs, present in every single AD patient, form in the most vulnerable neurons of the brain before spreading to other regions. Addressing this question is crucial to the design of novel therapeutics for the earliest stages of AD.

STAR★METHODS

Detailed methods are provided in the online version of this paper and include the following:

- KEY RESOURCES TABLE
- RESOURCE AVAILABILITY
  - Lead Contact
  - Materials Availability
  - Data and Code Availability
- EXPERIMENTAL MODEL AND SUBJECT DETAILS
  - *In vivo* animal studies
  - Mouse genotyping
  - Cell culture
- METHOD DETAILS
  - bacTRAP transgene construction
  - Detail of the bacTRAP mice analyzed
  - Cell type-specific molecular profiling
  - Histology
  - Comparison of the bacTRAP profiles with Allen Brain Atlas
  - Cell culture
  - Protein and RNA extraction from brain lysates
  - Tau splicing analysis
  - Western blot
  - Stereotaxic injections
  - RNA-seq analysis
  - Spatial homology analysis
  - Construction of functional networks
  - Gold standard
  - Human data compendium
  - Data integration
  - Network connectivity analysis
  - NetWAS 2.0 on AD GWAS
  - Establishment of the expert-curated gene set
  - Analysis of NetWAS 2.0 predictions
- QUANTIFICATION AND STATISTICAL ANALYSIS
- ADDITIONAL RESOURCES

AUTHOR CONTRIBUTIONS

J.-P.R., V.Y., O.G.T., and P.G. conceived and designed the research with input from M.H. and P.R.H. J.-P.R. generated mice with help from E.F.S., N.H., and L.B. J.-P.R., S.K., and C.A. performed bacTRAP experiments. P.R.-R. and Z.P. performed stereotaxic injections. V.Y. and O.G.T. conceived the computational analyses. V.Y. performed all bacTRAP data analyses, generated and analyzed functional networks, reprioritized genes, and re-analyzed publicly available datasets. W.W. performed some additional RNA-seq experiments. V.Y. and J.-P.R. analyzed results from the computational analyses. M.F., R.O., J.R., and K.D. curated amyloid and NFT lists. V.Y., R.D., and A.T. made the data available at http://alz.princeton.edu. J.-P.R., V.Y., O.G.T., and P.G. wrote the manuscript with input from M.F., P.R.H., P.R.-R., and A.B.-C.

DECLARATION OF INTERESTS

The authors declare no competing interests.

REFERENCES

Abromov, E., Doley, I., Fogel, H., Ciccotosto, G.D., Ruff, E., and Slutsky, I. (2009). Amyloid-beta as a positive endogenous regulator of release probability at hippocampal synapses. Nat. Neurosci. 12, 1567–1576.

Anders, S., Pyl, P.T., and Huber, W. (2015). HTSeq–a Python framework to work with high-throughput sequencing data. Bioinformatics 31, 166–169.

Anders, S., Reyes, A., and Huber, W. (2012). Detecting differential usage of exons from RNA-seq data. Genome Research 22, 4025.

Andorfer, C., Kress, Y., Espinoza, M., de Silva, R., Tucker, K.L., Barde, Y.-A., Duff, K., and Davies, P. (2003). Hyperphosphorylation and aggregation of tau in mice expressing normal human tau isoforms. J. Neurochem. 86, 582–590.

Apicco, D.J., Ash, P.E.A., Maziuk, B., LeBlang, C., Medalla, M., Al Abdullatif, A., Ferragud, A., Botelho, E., Ballance, H.I., Dhawan, U., et al. (2018). Reducing the RNA binding protein TIA1 protects against tau-mediated neurodegeneration in vivo. Nat. Neurosci. 21, 72–80.

Arnold, S.E., Hyman, B.T., Flory, J., Damasio, A.R., and Van Hoesen, G.W. (1991). The topographical and neuroanatomical distribution of neurofibrillary tangles and neuritic plaques in the cerebral cortex of patients with Alzheimer's disease. Cereb. Cortex 1, 103–116.

Arriagada, P.V., Growdon, J.H., Hedley-Whyte, E.T., and Hyman, B.T. (1992). Neurofibrillary tangles but not senile plaques parallel duration and severity of Alzheimer's disease. Neurology 42, 631–639.

Ayata, P., Badimon, A., Strasburger, H.J., Duff, M.K., Montgomery, S.E., Loh, Y.E., Ebert, A., Pimenova, A.A., Ramirez, B.R., Chan, A.T., et al. (2018). Epigenetic regulation of brain region-specific microglia clearance activity. Nat. Neurosci. 21, 1049–1060.

Bailey, T.L., Johnson, J., Grant, C.E., and Noble, W.S. (2015). The MEME Suite. Nucleic Acids Res. 43 (W1), W39–W49.

Bakker, A., Krauss, G.L., Albert, M.S., Speck, C.L., Jones, L.R., Stark, C.E., Yassa, M.A., Bassett, S.S., Shelton, A.L., and Gallagher, M. (2012). Reduction of hippocampal hyperactivity improves cognition in amnestic mild cognitive impairment. Neuron 74, 467–474.

Barrett, T., Wilhite, S.E., Ledoux, P., Evangelista, C., Kim, I.F., Tomashevsky, M., Marshall, K.A., Phillippy, K.H., Sherman, P.M., Holko, M., et al. (2013). NCBI GEO: archive for functional genomics data sets–update. Nucleic Acids Res. 41, D991–D995.

Bastian, M., Heymann, S., and Jacomy, M. (2009). Gephi: an open source software for exploring and manipulating networks. AAAI.

Beecham, G.W., Hamilton, K., Naj, A.C., Martin, E.R., Huentelman, M., Myers, A.J., Corneveaux, J.J., Hardy, J., Vonsattel, J.-P., Younkin, S.G., et al.; Alzheimer's Disease Genetics Consortium (ADGC) (2014). Genome-wide association meta-analysis of neuropathologic features of Alzheimer's disease and related dementias. PLoS Genet. 10, e1004606.

Blondel, V.D., Guillaume, J.-L., Lambiotte, R., and Lefebvre, E. (2008). Fast unfolding of communities in large networks. J. Stat. Mech. 2008, P10008.

Bodaleo, F.J., and Gonzalez-Billault, C. (2016). The Presynaptic Microtubule Cytoskeleton in Physiological and Pathological Conditions: Lessons from Drosophila Fragile X Syndrome and Hereditary Spastic Paraplegias. Front. Mol. Neurosci. 9, 60.

Borchelt, D.R., Ratovitski, T., van Lare, J., Lee, M.K., Gonzales, V., Jenkins, N.A., Copeland, N.G., Price, D.L., and Sisodia, S.S. (1997). Accelerated amyloid deposition in the brains of transgenic mice coexpressing mutant presenilin 1 and amyloid precursor proteins. Neuron 19, 939–945.

Boutz, P.L., Stoilov, P., Li, Q., Lin, C.-H., Chawla, G., Ostrow, K., Shiue, L., Ares, M., Jr., and Black, D.L. (2007). A post-transcriptional regulatory switch in polypyrimidine tract-binding proteins reprograms alternative splicing in developing neurons. Genes Dev. 21, 1636–1652.

Braak, H., and Braak, E. (1991). Neuropathological staging of Alzheimer-related changes. Acta Neuropathol. 82, 239–259.

Brichta, L., Shin, W., Jackson-Lewis, V., Blesa, J., Yap, E.-L., Walker, Z., Zhang, J., Roussarie, J.P., Alvarez, M.J., Califano, A., et al. (2015). Identification of neurodegenerative factors using translatome-regulatory network analysis. Nat. Neurosci. 18, 1325–1333.

Brier, M.R., Gordon, B., Friedrichsen, K., McCarthy, J., Stern, A., Christensen, J., Owen, C., Aldea, P., Su, Y., Hassenstab, J., et al. (2016). Tau and Aβ imaging, CSF measures, and cognition in Alzheimer's disease. Sci. Transl. Med. 8, 338ra66.

Bussière, T., Giannakopoulos, P., Bouras, C., Perl, D.P., Morrison, J.H., and Hof, P.R. (2003). Progressive degeneration of nonphosphorylated neurofilament protein-enriched pyramidal neurons predicts cognitive impairment in

Alzheimer's disease: stereologic analysis of prefrontal cortex area 9. J. Comp. Neurol. 463, 281–302.

Caraci, F., Battaglia, G., Busceti, C., Biagioni, F., Mastroiacovo, F., Bosco, P., Drago, F., Nicoletti, F., Sortino, M.A., and Copani, A. (2008). TGF-beta 1 protects against Abeta-neurotoxicity via the phosphatidylinositol-3-kinase pathway. Neurobiol. Dis. 30, 234–242.

Carlyle, B.C., Kitchen, R.R., Kanyo, J.E., Voss, E.Z., Pletikos, M., Sousa, A.M.M., Lam, T.T., Gerstein, M.B., Sestan, N., and Nairn, A.C. (2017). A multiregional proteomic survey of the postnatal human brain. Nat. Neurosci. 20, 1787–1795.

Cembrowski, M.S., Wang, L., Sugino, K., Shields, B.C., and Spruston, N. (2016). Hipposeq: a comprehensive RNA-seq database of gene expression in hippocampal principal neurons. eLife 5, e14997.

Chatr-Aryamontri, A., Breitkreutz, B.-J., Heinicke, S., Boucher, L., Winter, A., Stark, C., Nixon, J., Ramage, L., Kolas, N., O'Donnell, L., et al. (2013). The BioGRID interaction database: 2013 update. Nucleic Acids Res. 41, D816–D823.

Chibnik, L.B., White, C.C., Mukherjee, S., Raj, T., Yu, L., Larson, E.B., Montine, T.J., Keene, C.D., Sonnen, J., Schneider, J.A., et al. (2018). Susceptibility to neurofibrillary tangles: role of the PTPRD locus and limited pleiotropy with other neuropathologies. Mol. Psychiatry 23, 1521–1529.

Clarke, L.E., Liddelow, S.A., Chakraborty, C., Münch, A.E., Heiman, M., and Barres, B.A. (2018). Normal aging induces A1-like astrocyte reactivity. Proc. Natl. Acad. Sci. USA 115, E1896–E1905.

Coppola, G., Chinnathambi, S., Lee, J.J., Dombroski, B.A., Baker, M.C., Soto-Ortolaza, A.I., Lee, S.E., Klein, E., Huang, A.Y., Sears, R., et al.; Alzheimer's Disease Genetics Consortium (2012). Evidence for a role of the rare p.A152T variant in MAPT in increasing the risk for FTD-spectrum and Alzheimer's diseases. Hum. Mol. Genet. 21, 3500–3512.

Deming, Y., Li, Z., Kapoor, M., Harari, O., Del-Aguila, J.L., Black, K., Carrell, D., Cai, Y., Fernandez, M.V., Budde, J., et al.; Alzheimer's Disease Neuroimaging Initiative (ADNI); Alzheimer Disease Genetic Consortium (ADGC) (2017). Genome-wide association study identifies four novel loci associated with Alzheimer's endophenotypes and disease modifiers. Acta Neuropathol. 133, 839–856.

Desikan, R.S., Schork, A.J., Wang, Y., Witoelar, A., Sharma, M., McEvoy, L.K., Holland, D., Brewer, J.B., Chen, C.-H., Thompson, W.K., et al.; ADNI, ADGC, GERAD, CHARGE and IPDGC Investigators (2015). Genetic overlap between Alzheimer's disease and Parkinson's disease at the MAPT locus. Mol. Psychiatry 20, 1588–1595.

Dobin, A., Davis, C.A., Schlesinger, F., Drenkow, J., Zaleski, C., Jha, S., Batut, P., Chaisson, M., and Gingeras, T.R. (2013). STAR: ultrafast universal RNA-seq aligner. Bioinformatics 29, 15–21.

Doyle, J.P., Dougherty, J.D., Heiman, M., Schmidt, E.F., Stevens, T.R., Ma, G., Bupp, S., Shrestha, P., Shah, R.D., Doughty, M.L., et al. (2008). Application of a translational profiling approach for the comparative analysis of CNS cell types. Cell 135, 749–762.

Du, H., Guo, L., Yan, S., Sosunov, A.A., McKhann, G.M., and Yan, S.S. (2010). Early deficits in synaptic mitochondria in an Alzheimer's disease mouse model. Proc. Natl. Acad. Sci. USA 107, 18670–18675.

Duff, K., Knight, H., Refolo, L.M., Sanders, S., Yu, X., Picciano, M., Malester, B., Hutton, M., Adamson, J., Goedert, M., et al. (2000). Characterization of pathology in transgenic mice over-expressing human genomic and cDNA tau transgenes. Neurobiol. Dis. 7, 87–98.

Dugas-Ford, J., Rowell, J.J., and Ragsdale, C.W. (2012). Cell-type homologies and the origins of the neocortex. Proc. Natl. Acad. Sci. USA 109, 16974–16979.

Dunckley, T., Beach, T.G., Ramsey, K.E., Grover, A., Mastroeni, D., Walker, D.G., LaFleur, B.J., Coon, K.D., Brown, K.M., Caselli, R., et al. (2006). Gene expression correlates of neurofibrillary tangles in Alzheimer's disease. Neurobiol. Aging 27, 1359–1371.

Efthymiou, A.G., and Goate, A.M. (2017). Late onset Alzheimer's disease genetics implicates microglial pathways in disease risk. Mol. Neurodegener. 12, 43.

Emmer, K.L., Waxman, E.A., Covy, J.P., and Giasson, B.I. (2011). E46K human alpha-synuclein transgenic mice develop Lewy-like and tau pathology associated with age-dependent, detrimental motor impairment. J. Biol. Chem. 286, 35104–35118.

Fukutani, Y., Cairns, N.J., Shiozawa, M., Sasaki, K., Sudo, S., Isaki, K., and Lantos, P.L. (2000). Neuronal loss and neurofibrillary degeneration in the hippocampal cortex in late-onset sporadic Alzheimer's disease. Psychiatry Clin. Neurosci. 54, 523–529.

Furlanis, E., Traunmüller, L., Fucile, G., and Scheiffele, P. (2019). Landscape of ribosome-engaged transcript isoforms reveals extensive neuronal-cell-class-specific alternative splicing programs. Nat. Neurosci. 22, 1709–1717.

Giannakopoulos, P., Herrmann, F.R., Bussière, T., Bouras, C., Kövari, E., Perl, D.P., Morrison, J.H., Gold, G., and Hof, P.R. (2003). Tangle and neuron numbers, but not amyloid load, predict cognitive status in Alzheimer's disease. Neurology 60, 1495–1500.

Giasson, B.I., Forman, M.S., Higuchi, M., Golbe, L.I., Graves, C.L., Kotzbauer, P.T., Trojanowski, J.Q., and Lee, V.M.-Y. (2003). Initiation and synergistic fibrillization of tau and alpha-synuclein. Science 300, 636–640.

Gómez-Isla, T., Price, J.L., McKeel, D.W., Jr., Morris, J.C., Growdon, J.H., and Hyman, B.T. (1996). Profound loss of layer II entorhinal cortex neurons occurs in very mild Alzheimer's disease. J. Neurosci. 16, 4491–4500.

Gong, S., Zheng, C., Doughty, M.L., Losos, K., Didkovsky, N., Schambra, U.B., Nowak, N.J., Joyner, A., Leblanc, G., Hatten, M.E., and Heintz, N. (2003). A gene expression atlas of the central nervous system based on bacterial artificial chromosomes. Nature 425, 917–925.

Grant, C.E., Bailey, T.L., and Noble, W.S. (2011). FIMO: scanning for occurrences of a given motif. Bioinformatics 27, 1017–1018.

Gray, J.D., Rubin, T.G., Kogan, J.F., Marrocco, J., Weidmann, J., Lindkvist, S., Lee, F.S., Schmidt, E.F., and McEwen, B.S. (2018). Translational profiling of stress-induced neuroplasticity in the CA3 pyramidal neurons of BDNF Val66Met mice. Mol. Psychiatry 23, 904–913.

Greene, C.S., Krishnan, A., Wong, A.K., Ricciotti, E., Zelaya, R.A., Himmelstein, D.S., Zhang, R., Hartmann, B.M., Zaslavsky, E., Sealfon, S.C., et al. (2015). Understanding multicellular function and disease with human tissue-specific networks. Nat. Genet. 47, 569–576.

Guo, T., Noble, W., and Hanger, D.P. (2017). Roles of tau protein in health and disease. Acta Neuropathol. 133, 665–704.

Hamilton, R.L. (2000). Lewy bodies in Alzheimer's disease: a neuropathological review of 145 cases using alpha-synuclein immunohistochemistry. Brain Pathol. 10, 378–384.

Hara, M., Hirokawa, K., Kamei, S., and Uchihara, T. (2013). Isoform transition from four-repeat to three-repeat tau underlies dendrosomatic and regional progression of neurofibrillary pathology. Acta Neuropathol. 125, 565–579.

Hawrylycz, M.J., Lein, E.S., Guillozet-Bongaarts, A.L., Shen, E.H., Ng, L., Miller, J.A., van de Lagemaat, L.N., Smith, K.A., Ebbert, A., Riley, Z.L., et al. (2012). An anatomically comprehensive atlas of the adult human brain transcriptome. Nature 489, 391–399.

Hawrylycz, M., Miller, J.A., Menon, V., Feng, D., Dolbeare, T., Guillozet-Bongaarts, A.L., Jegga, A.G., Aronow, B.J., Lee, C.-K., Bernard, A., et al. (2015). Canonical genetic signatures of the adult human brain. Nat. Neurosci. 18, 1832–1844.

Heiman, M., Schaefer, A., Gong, S., Peterson, J.D., Day, M., Ramsey, K.E., Suárez-Fariñas, M., Schwarz, C., Stephan, D.A., Surmeier, D.J., et al. (2008). A translational profiling approach for the molecular characterization of CNS cell types. Cell 135, 738–748.

Hof, P.R., and Morrison, J.H. (1990). Quantitative analysis of a vulnerable subset of pyramidal neurons in Alzheimer's disease: II. Primary and secondary visual cortex. J. Comp. Neurol. 301, 55–64.

Huang, H., Arighi, C.N., Ross, K.E., Ren, J., Li, G., Chen, S.-C., Wang, Q., Cowart, J., Vijay-Shanker, K., and Wu, C.H. (2018). iPTMnet: an integrated

resource for protein post-translational modification network discovery. Nucleic Acids Res. *46* (D1), D542–D550.

Huttenhower, C., Schroeder, M., Chikina, M.D., and Troyanskaya, O.G. (2008). The Sleipnir library for computational functional genomics. Bioinformatics *24*, 1559–1561.

Hyman, B.T., Van Hoesen, G.W., Damasio, A.R., and Barnes, C.L. (1984). Alzheimer's disease: cell-specific pathology isolates the hippocampal formation. Science *225*, 1168–1170.

Iseki, E., Yamamoto, R., Murayama, N., Minegishi, M., Togo, T., Katsuse, O., Kosaka, K., Akiyama, H., Tsuchiya, K., de Silva, R., et al. (2006). Immunohistochemical investigation of neurofibrillary tangles and their tau isoforms in brains of limbic neurofibrillary tangle dementia. Neurosci. Lett. *405*, 29–33.

Joachims, T. (2005). A support vector method for multi-variate performance measures. Proceedings of the 22nd International Conference on Machine Learning. (ACM Press), pp. 377–384.

Kaufman, S.K., Del Tredici, K., Thomas, T.L., Braak, H., and Diamond, M.I. (2018). Tau seeding activity begins in the transentorhinal/entorhinal regions and anticipates phospho-tau pathology in Alzheimer's disease and PART. Acta Neuropathol. *136*, 57–67.

Khandelwal, P.J., Dumanis, S.B., Feng, L.R., Maguire-Zeiss, K., Rebeck, G., Lashuel, H.A., and Moussa, C.E. (2010). Parkinson-related parkin reduces α-Synuclein phosphorylation in a gene transfer model. Mol. Neurodegener. *5*, 47.

Khandelwal, P.J., Dumanis, S.B., Herman, A.M., Rebeck, G.W., and Moussa, C.E.-H. (2012). Wild type and P301L mutant Tau promote neuro-inflammation and α-Synuclein accumulation in lentiviral gene delivery models. Mol. Cell. Neurosci. *49*, 44–53.

Kim, S., Kwon, D., Shin, S.-Y., and Wilbur, W.J. (2012). PIE the search: searching PubMed literature for protein interaction information. Bioinformatics *28*, 597–598.

Kohara, K., Pignatelli, M., Rivest, A.J., Jung, H.-Y., Kitamura, T., Suh, J., Frank, D., Kajikawa, K., Mise, N., Obata, Y., et al. (2014). Cell type-specific genetic and optogenetic tools reveal hippocampal CA2 circuits. Nat. Neurosci. *17*, 269–279.

Kramarz, B., Roncaglia, P., Meldal, B.H.M., Huntley, R.P., Martin, M.J., Orchard, S., Parkinson, H., Brough, D., Bandopadhyay, R., Hooper, N.M., and Lovering, R.C. (2018). Improving the Gene Ontology Resource to Facilitate More Informative Analysis and Interpretation of Alzheimer's Disease Data. Genes (Basel) *9*, 593.

Krishnan, A., Zhang, R., Yao, V., Theesfeld, C.L., Wong, A.K., Tadych, A., Volfovsky, N., Packer, A., Lash, A., and Troyanskaya, O.G. (2016). Genome-wide prediction and functional characterization of the genetic basis of autism spectrum disorder. Nat. Neurosci. *19*, 1454–1462.

Lambert, J.C., Ibrahim-Verbaas, C.A., Harold, D., Naj, A.C., Sims, R., Bellenguez, C., DeStafano, A.L., Bis, J.C., Beecham, G.W., Grenier-Boley, B., et al.; European Alzheimer's Disease Initiative (EADI); Genetic and Environmental Risk in Alzheimer's Disease; Alzheimer's Disease Genetic Consortium; Cohorts for Heart and Aging Research in Genomic Epidemiology (2013). Meta-analysis of 74,046 individuals identifies 11 new susceptibility loci for Alzheimer's disease. Nat. Genet. *45*, 1452–1458.

Lein, E.S., Hawrylycz, M.J., Ao, N., Ayres, M., Bensinger, A., Bernard, A., Boe, A.F., Boguski, M.S., Brockway, K.S., Byrnes, E.J., et al. (2007). Genome-wide atlas of gene expression in the adult mouse brain. Nature *445*, 168–176.

Lein, E.S., Zhao, X., and Gage, F.H. (2004). Defining a molecular atlas of the hippocampus using DNA microarrays and high-throughput in situ hybridization. J. Neurosci. *24*, 3879–3889.

Lewis, D.A., Campbell, M.J., Terry, R.D., and Morrison, J.H. (1987). Laminar and regional distributions of neurofibrillary tangles and neuritic plaques in Alzheimer's disease: a quantitative study of visual and auditory cortices. J. Neurosci. *7*, 1799–1808.

Liang, W.S., Dunckley, T., Beach, T.G., Grover, A., Mastroeni, D., Walker, D.G., Caselli, R.J., Kukull, W.A., McKeel, D., Morris, J.C., et al. (2007). Gene expression profiles in anatomically and functionally distinct regions of the normal aged human brain. Physiol. Genomics *28*, 311–322.

Lewis, T.L., Courchet, J., and Polleux, F. (2013). Cell biology in neuroscience: Cellular and molecular mechanisms underlying axon formation, growth, and branching. J. Cell Biol. *202*, 837–848.

Liang, W.S., Dunckley, T., Beach, T.G., Grover, A., Mastroeni, D., Ramsey, K., Caselli, R.J., Kukull, W.A., McKeel, D., Morris, J.C., et al. (2008). Altered neuronal gene expression in brain regions differentially affected by Alzheimer's disease: a reference data set. Physiol. Genomics *33*, 240–256.

Licata, L., Briganti, L., Peluso, D., Perfetto, L., Iannuccelli, M., Galeota, E., Sacco, F., Palma, A., Nardozza, A.P., Santonico, E., et al. (2012). MINT, the molecular interaction database: 2012 update. Nucleic Acids Res. *40*, D857–D861.

Liu, F., and Gong, C.-X. (2008). Tau exon 10 alternative splicing and tauopathies. Mol. Neurodegener. *3*, 8.

Liu, M., Pleasure, S.J., Collins, A.E., Noebels, J.L., Naya, F.J., Tsai, M.J., and Lowenstein, D.H. (2000). Loss of BETA2/NeuroD leads to malformation of the dentate gyrus and epilepsy. Proc. Natl. Acad. Sci. USA *97*, 865–870.

Liu, C.-C., Tsai, C.-W., Deak, F., Rogers, J., Penuliar, M., Sung, Y.M., Maher, J.N., Fu, Y., Li, X., Xu, H., et al. (2014). Deficiency in LRP6-mediated Wnt signaling contributes to synaptic abnormalities and amyloid pathology in Alzheimer's disease. Neuron *84*, 63–77.

Llorian, M., Schwartz, S., Clark, T.A., Hollander, D., Tan, L.-Y., Spellman, R., Gordon, A., Schweitzer, A.C., de la Grange, P., Ast, G., and Smith, C.W. (2010). Position-dependent alternative splicing activity revealed by global profiling of alternative splicing events regulated by PTB. Nat. Struct. Mol. Biol. *17*, 1114–1123.

Mathelier, A., Zhao, X., Zhang, A.W., Parcy, F., Worsley-Hunt, R., Arenillas, D.J., Buchman, S., Chen, C., Chou, A., Ienasescu, H., et al. (2014). JASPAR 2014: an extensively expanded and updated open-access database of transcription factor binding profiles. Nucleic Acids Res. *42*, D142–D147.

Mewes, H.W., Ruepp, A., Theis, F., Rattei, T., Walter, M., Frishman, D., Suhre, K., Spannagl, M., Mayer, K.F.X., Stümpflen, V., and Antonov, A. (2011). MIPS: curated databases and comprehensive secondary data resources in 2010. Nucleic Acids Res. *39*, D220–D224.

Miller, J.A., Oldham, M.C., and Geschwind, D.H. (2008). A systems level analysis of transcriptional changes in Alzheimer's disease and normal aging. J. Neurosci. *28*, 1410–1420.

Miller, J.A., Woltjer, R.L., Goodenbour, J.M., Horvath, S., and Geschwind, D.H. (2013). Genes and pathways underlying regional and cell type changes in Alzheimer's disease. Genome Med. *5*, 48.

Miller, J.A., Guillozet-Bongaarts, A., Gibbons, L.E., Postupna, N., Renz, A., Beller, A.E., Sunkin, S.M., Ng, L., Rose, S.E., Smith, K.A., et al. (2017). Neuropathological and transcriptomic characteristics of the aged brain. eLife *6*, 383.

Mishra, A., and Macgregor, S. (2015). VEGAS2: Software for More Flexible Gene-Based Testing. Twin Res. Hum. Genet. *18*, 86–91.

Morrison, J.H., and Hof, P.R. (1997). Life and death of neurons in the aging brain. Science *278*, 412–419.

Mostafavi, S., Gaiteri, C., Sullivan, S.E., White, C.C., Tasaki, S., Xu, J., Taga, M., Klein, H.-U., Patrick, E., Komashko, V., et al. (2018). A molecular network of the aging human brain provides insights into the pathology and cognitive decline of Alzheimer's disease. Nat. Neurosci. *21*, 811–819.

Moussaud, S., Jones, D.R., Moussaud-Lamodière, E.L., Delenclos, M., Ross, O.A., and McLean, P.J. (2014). Alpha-synuclein and tau: teammates in neurodegeneration? Mol. Neurodegener. *9*, 43.

Nagahara, A.H., Merrill, D.A., Coppola, G., Tsukada, S., Schroeder, B.E., Shaked, G.M., Wang, L., Blesch, A., Kim, A., Conner, J.M., et al. (2009). Neuroprotective effects of brain-derived neurotrophic factor in rodent and primate models of Alzheimer's disease. Nat. Med. *15*, 331–337.

Orchard, S., Ammari, M., Aranda, B., Breuza, L., Briganti, L., Broackes-Carter, F., Campbell, N.H., Chavali, G., Chen, C., del-Toro, N., et al. (2014). The

MIntAct project–IntAct as a common curation platform for 11 molecular interaction databases. Nucleic Acids Res. 42, D358–D363.

Oughtred, R., Stark, C., Breitkreutz, B.-J., Rust, J., Boucher, L., Chang, C., Kolas, N., O'Donnell, L., Leung, G., McAdam, R., et al. (2019). The BioGRID interaction database: 2019 update. Nucleic Acids Res. 47 (D1), D529–D541.

Palop, J.J., and Mucke, L. (2010). Amyloid-beta-induced neuronal dysfunction in Alzheimer's disease: from synapses toward neural networks. Nat. Neurosci. 13, 812–818.

Park, C.Y., Wong, A.K., Greene, C.S., Rowland, J., Guan, Y., Bongo, L.A., Burdine, R.D., and Troyanskaya, O.G. (2013). Functional knowledge transfer for high-accuracy prediction of under-studied biological processes. PLoS Comput. Biol. 9, e1002957.

Pesold, C., Impagnatiello, F., Pisu, M.G., Uzunov, D.P., Costa, E., Guidotti, A., and Caruncho, H.J. (1998). Reelin is preferentially expressed in neurons synthesizing gamma-aminobutyric acid in cortex and hippocampus of adult rats. Proc. Natl. Acad. Sci. USA 95, 3221–3226.

Ramaswami, M., Taylor, J.P., and Parker, R. (2013). Altered ribostasis: RNA-protein granules in degenerative disorders. Cell 154, 727–736.

Robinson, M.D., McCarthy, D.J., and Smyth, G.K. (2010). edgeR: a Bioconductor package for differential expression analysis of digital gene expression data. Bioinformatics 26, 139–140.

Sanz, E., Yang, L., Su, T., Morris, D.R., McKnight, G.S., and Amieux, P.S. (2009). Cell-type-specific isolation of ribosome-associated mRNA from complex tissues. Proc. Natl. Acad. Sci. USA 106, 13939–13944.

Saxena, S., and Caroni, P. (2011). Selective neuronal vulnerability in neurodegenerative diseases: from stressor thresholds to degeneration. Neuron 71, 35–48.

Scheckel, C., Drapeau, E., Frias, M.A., Park, C.Y., Fak, J., Zucker-Scharff, I., Kou, Y., Haroutunian, V., Ma'ayan, A., Buxbaum, J.D., and Darnell, R.B. (2016). Regulatory consequences of neuronal ELAV-like protein binding to coding and non-coding RNAs in human brain. eLife 5, 4625.

Sepulcre, J., Grothe, M.J., Sabuncu, M., Chhatwal, J., Schultz, A.P., Hanseeuw, B., El Fakhri, G., Sperling, R., and Johnson, K.A. (2017). Hierarchical Organization of Tau and Amyloid Deposits in the Cerebral Cortex. JAMA Neurol. 74, 813–820.

Silva, M.C., Cheng, C., Mair, W., Almeida, S., Fong, H., Biswas, M.H.U., Zhang, Z., Huang, Y., Temple, S., Coppola, G., et al. (2016). Human iPSC-Derived Neuronal Model of Tau-A152T Frontotemporal Dementia Reveals Tau-Mediated Mechanisms of Neuronal Vulnerability. Stem Cell Reports 7, 325–340.

Small, S.A., Kent, K., Pierce, A., Leung, C., Kang, M.S., Okada, H., Honig, L., Vonsattel, J.-P., and Kim, T.-W. (2005). Model-guided microarray implicates the retromer complex in Alzheimer's disease. Ann. Neurol. 58, 909–919.

Smyth, G.K. (2004). Linear models and empirical bayes methods for assessing differential expression in microarray experiments. Stat. Appl. Genet. Mol. Biol. 3, 3.

Song, A., Yan, J., Kim, S., Risacher, S.L., Wong, A.K., Saykin, A.J., Shen, L., and Greene, C.S.; Alzheimer's Disease Neuroimaging Initiative (2016). Network-based analysis of genetic variants associated with hippocampal volume in Alzheimer's disease: a study of ADNI cohorts. BioData Min. 9, 3.

Stark, C., Breitkreutz, B.-J., Reguly, T., Boucher, L., Breitkreutz, A., and Tyers, M. (2006). BioGRID: a general repository for interaction datasets. Nucleic Acids Res. 34, D535–D539.

Strand, A.D., Aragaki, A.K., Baquet, Z.C., Hodges, A., Cunningham, P., Holmans, P., Jones, K.R., Jones, L., Kooperberg, C., and Olson, J.M. (2007). Conservation of regional gene expression in mouse and human brain. PLoS Genet. 3, e59.

Subramanian, A., Tamayo, P., Mootha, V.K., Mukherjee, S., Ebert, B.L., Gillette, M.A., Paulovich, A., Pomeroy, S.L., Golub, T.R., Lander, E.S., and Mesirov, J.P. (2005). Gene set enrichment analysis: a knowledge-based approach for interpreting genome-wide expression profiles. Proc. Natl. Acad. Sci. USA 102, 15545–15550.

Sun, S., Sun, Y., Ling, S.-C., Ferraiuolo, L., McAlonis-Downes, M., Zou, Y., Drenner, K., Wang, Y., Ditsworth, D., Tokunaga, S., et al. (2015). Translational profiling identifies a cascade of damage initiated in motor neurons and spreading to glia in mutant SOD1-mediated ALS. Proc. Natl. Acad. Sci. USA 112, E6993–E7002.

Tamamaki, N., and Nojyo, Y. (1993). Projection of the entorhinal layer II neurons in the rat as revealed by intracellular pressure-injection of neurobiotin. Hippocampus 3, 471–480.

Tesseur, I., Zou, K., Esposito, L., Bard, F., Berber, E., Can, J.V., Lin, A.H., Crews, L., Tremblay, P., Mathews, P., et al. (2006). Deficiency in neuronal TGF-beta signaling promotes neurodegeneration and Alzheimer's pathology. J. Clin. Invest. 116, 3060–3069.

Thal, D.R., Rüb, U., Orantes, M., and Braak, H. (2002). Phases of A beta-deposition in the human brain and its relevance for the development of AD. Neurology 58, 1791–1800.

Torii, M., Arighi, C.N., Li, G., Wang, Q., Wu, C.H., and Vijay-Shanker, K. (2015). RLIMS-P 2.0: A Generalizable Rule-Based Information Extraction System for Literature Mining of Protein Phosphorylation Information. IEEE/ACM Trans. Comput. Biol. Bioinformatics 12, 17–29.

Troyanskaya, O., Cantor, M., Sherlock, G., Brown, P., Hastie, T., Tibshirani, R., Botstein, D., and Altman, R.B. (2001). Missing value estimation methods for DNA microarrays. Bioinformatics 17, 520–525.

Vossel, K.A., Beagle, A.J., Rabinovici, G.D., Shu, H., Lee, S.E., Naasan, G., Hegde, M., Cornes, S.B., Henry, M.L., Nelson, A.B., et al. (2013). Seizures and epileptiform activity in the early stages of Alzheimer disease. JAMA Neurol. 70, 1158–1166.

Walker, L.C., and Jucker, M. (2017). The Exceptional Vulnerability of Humans to Alzheimer's Disease. Trends Mol. Med. 23, 534–545.

Wamsley, B., Jaglin, X.H., Favuzzi, E., Quattrocolo, G., Nigro, M.J., Yusuf, N., Khodadadi-Jamayran, A., Rudy, B., and Fishell, G. (2018). Rbfox1 Mediates Cell-type-Specific Splicing in Cortical Interneurons. Neuron 100, 846–859.e7.

Wang, J., Gao, Q.-S., Wang, Y., Lafyatis, R., Stamm, S., and Andreadis, A. (2004). Tau exon 10, whose missplicing causes frontotemporal dementia, is regulated by an intricate interplay of cis elements and trans factors. J. Neurochem. 88, 1078–1090.

West, M.J., Coleman, P.D., Flood, D.G., and Troncoso, J.C. (1994). Differences in the pattern of hippocampal neuronal loss in normal ageing and Alzheimer's disease. Lancet 344, 769–772.

Wollerton, M.C., Gooding, C., Wagner, E.J., Garcia-Blanco, M.A., and Smith, C.W.J. (2004). Autoregulation of polypyrimidine tract binding protein by alternative splicing leading to nonsense-mediated decay. Mol. Cell 13, 91–100.

Yeom, K.-H., Mitchell, S., Linares, A.J., Zheng, S., Lin, C.-H., Wang, X.-J., Hoffmann, A., and Black, D.L. (2018). Polypyrimidine tract-binding protein blocks miRNA-124 biogenesis to enforce its neuronal-specific expression in the mouse. Proc. Natl. Acad. Sci. USA 115, E11061–E11070.

Zeng, H., Shen, E.H., Hohmann, J.G., Oh, S.W., Bernard, A., Royall, J.J., Glattfelder, K.J., Sunkin, S.M., Morris, J.A., Guillozet-Bongaarts, A.L., et al. (2012). Large-scale cellular-resolution gene profiling in human neocortex reveals species-specific molecular signatures. Cell 149, 483–496.

Zhang, B., Gaiteri, C., Bodea, L.-G., Wang, Z., McElwee, J., Podtelezhnikov, A.A., Zhang, C., Xie, T., Tran, L., Dobrin, R., et al. (2013). Integrated systems approach identifies genetic nodes and networks in late-onset Alzheimer's disease. Cell 153, 707–720.

Zheng, S., Gray, E.E., Chawla, G., Porse, B.T., O'Dell, T.J., and Black, D.L. (2012). PSD-95 is post-transcriptionally repressed during early neural development by PTBP1 and PTBP2. Nat. Neurosci. 15 (S1), 381–388.

STAR★METHODS

KEY RESOURCES TABLE

REAGENT or RESOURCE	SOURCE	IDENTIFIER
Antibodies		
goat anti PTBP1 polyclonal antibody	abcam	Abcam Cat# ab5642; RRID:AB_305011
monoclonal anti EGFP antibody Htz-19C8 (for bacTRAP), bioreactor supernatant	Memorial Sloan Kettering Cancer Center - Monoclonal Antibody Facility	Cat# HtzGFP-19C8; RRID: NA
monoclonal anti EGFP antibody Htz-19F7 (for bacTRAP), bioreactor supernatant	Memorial Sloan Kettering Cancer Center - Monoclonal Antibody Facility	Cat# HtzGFP-19F7; RRID: NA
chicken anti GFP polyclonal antibody (for immunofluorescence)	abcam	Abcam Cat# ab13970; RRID:AB_300798
Alexa 488-donkey anti-chicken secondary antibody	Thermo Fisher Scientific	Thermo Fisher Scientific Cat# A-11039; RRID:AB_2534096
IRDye 680RD Donkey anti-Goat IgG, secondary antibody	Li-COR Biosciences	LI-COR Biosciences Cat# 926-68074; RRID:AB_10956736
IRDye 800CW Donkey anti-Mouse IgG, secondary antibody	Li-COR Biosciences	LI-COR Biosciences Cat# 926-32212; RRID:AB_621847
IRDye 800CW Donkey anti-Goat IgG, secondary antibody	Li-COR Biosciences	LI-COR Biosciences Cat# 926-32214; RRID:AB_621846
IRDye 680RD Donkey anti-Mouse IgG, secondary antibody	Li-COR Biosciences	LI-COR Biosciences Cat# 926-68072; RRID:AB_10953628
mouse anti-β actin monoclonal antibody	Cell Signaling Technology	Cell Signaling Technology Cat# 3700; RRID:AB_2242334
Bacterial and Virus Strains		
AAV1-hSyn1-mPTBP1-IRES-mCherry carrying the NM_008956 cDNA for PTBP1	Vector biolabs	RRID: NA
AAV1-mCherry-U6-scrmb-shRNA 5′-CCGG-CAACAAGATGAAG AGCACCAACTCGAGTTGGTGC TCTTCATCTTGTTG-TTTTT-3′	Vector biolabs	RRID: NA
AAV1-mCherry-U6-mPTBP1-shRNA - shRNA sequence 5′-CCGG-CTCAA TGTCAAGTACAACAATCTCGAGAT TGTTGTACTTGACATTGAG-TTTTT −3′	Vector biolabs	RRID: NA
AAV1-hSyn1-mCherry-WPRE	Vector biolabs	RRID: NA
Critical Commercial Assays		
human MAPT, FAM/MGB Taqman probe spanning exons 11 and 12 (total tau)	Applied Biosystems	Assay ID Hs00902193_m1; RRID: NA
human SNCA, FAM/MGB Taqman probe	Applied Biosystems	Assay ID Hs00240906_m1; RRID: NA
mouse Ptbp1, FAM/MGB Taqman probe	Applied Biosystems	Assay ID Mm01731480_gH; RRID: NA
human PTBP1, FAM/MGB Taqman probe	Applied Biosystems	Assay ID Hs00738538_g1; RRID: NA

Continued

REAGENT or RESOURCE	SOURCE	IDENTIFIER
mouse gapdh, endogenous control, FAM/MGB Taqman probe	Applied Biosystems	Cat# 4352932E; RRID: NA
human gapdh, endogenous control, FAM/MGB Taqman probe	Applied Biosystems	Cat# 4333764F; RRID: NA
Accell non-targeting control pool	Horizon discovery (Dharmacon)	Cat# D-001910-10; RRID: NA
Accell human PTBP1 SMARTpool siRNA	Horizon discovery (Dharmacon)	Cat# E-003528-00; RRID: NA
human MAPT, FAM/MGB Taqman probe spanning exons 9 and 11 (3R-tau)	Applied Biosystems	Assay ID Hs00902192_m1; RRID: NA
human MAPT, FAM/MGB Taqman probe spanning exons 9 and 10 (4R-tau)	Applied Biosystems	Assay ID Hs00902312_m1; RRID: NA
Deposited Data		
Adult Changes in Thought, dataset of hippocampal samples of elderly individuals at risk for dementia with paired gene expression data and pathology measurements. Used for testing correlation between NetWAS 2.0 results and amyloid plaques and tau.	Miller et al., 2017	http://aging.brain-map.org/download/index
Liang et al. dataset of lasercapture microdissected ECII neurons in AD versus control: used for testing differential expression of NetWAS genes in ECII neurons of AD patients.	GEO, Liang et al., 2008	GSE5281, https://www.ncbi.nlm.nih.gov/geo/query/acc.cgi?acc=GSE5281
Agora AMP-AD: used for testing differential expression of PTB in the brain of AD patients.	https://agora.ampadportal.org/genes/(genes-router: gene-details/ENSG00000011304)	
JASPAR, part of the human data compendium for functional network construction.	Mathelier et al., 2014	http://jaspar.genereg.net/
MSigDB, part of the human data compendium for functional network construction.	Subramanian et al., 2005	https://www.gsea-msigdb.org/gsea/msigdb/
BioGRID, part of the human data compendium for functional network construction.	Chatr-Aryamontri et al., 2013	https://thebiogrid.org/
IntAct, part of the human data compendium for functional network construction.	Orchard et al., 2014	https://www.ebi.ac.uk/intact/
MINT, part of the human data compendium for functional network construction.	Licata et al., 2012	https://mint.bio.uniroma2.it/
MIPS, part of the human data compendium for functional network construction.	Mewes et al., 2011	https://mips.helmholtz-muenchen.de/proj/ppi/
Uncropped gel images for Figure 5 and Figure S3	Mendeley	https://dx.doi.org/10.17632/g67bhh7zsj.1
RNaseq data for the bacTRAP profiling of 7 neuron types at 5, 12 and 24 months of age, and the APP/PS1 ECII-bacTRAP profiles	GEO	GSE151460, https://www.ncbi.nlm.nih.gov/geo/query/acc.cgi?acc=GSE151460
RNaseq data for bacTRAP profiling of ECII neurons upon silencing and overexpression of Ptbp1 in the mouse EC.	GEO	GSE151356, https://www.ncbi.nlm.nih.gov/geo/query/acc.cgi?acc=GSE151356
Experimental Models: Cell Lines		
SH-SY5Y neuroblastoma cell line	ATCC	ATCC Cat# CRL-2266; RRID:CVCL_0019
Experimental Models: Organisms/Strains		
Mouse: wild-type mice: C57BL/6J	Jackson lab	IMSR Cat# JAX:000664; RRID:IMSR_JAX:000664

(Continued on next page)

Continued

REAGENT or RESOURCE	SOURCE	IDENTIFIER
Mouse: APP/PS1: B6.Cg-Tg(APPswe,PSEN1dE9)85Dbo/Mmjax	Jackson lab	MMRRC Stock No: 34832-JAX; RRID: NA
Mouse: Cck-bacTRAP: B6;FVB-Tg(Cck-EGFP/Rpl10a)GM391Htz/J	Jackson lab	IMSR Cat# JAX:030249; RRID:IMSR_JAX:030249
Mouse: Gprin3-bacTRAP	described in Gray et al., 2018	RRID: NA
Mouse: htau PAC: B6.Cg-$Mapt^{tm1(EGFP)Klt}$ Tg(MAPT)8cPdav/J	Jackson lab	IMSR Cat# JAX:005491; RRID:IMSR_JAX:005491
Oligonucleotides		
all mouse genotyping primers	See Table S7 for sequences	IDT-DNA; RRID: NA
fluorescent PCR for human tau splicing - forward primer	IDT-DNA	HPLC purified 5′-IRDye 800 – CTCCAAAATCAGG GGATCGC – 3′; RRID: NA
fluorescent PCR for human tau splicing - reverse primer	IDT-DNA	unlabeled 5′ – CCTTGCTC AGGTCAACTGGT – 3′; RRID: NA
fluorescent PCR for mouse tau splicing - forward primer	IDT-DNA	HPLC purified 5′-IRDye 800 – CACCAAAATCCG GAGAACGA – 3′; RRID: NA
fluorescent PCR for mouse tau splicing - reverse primer	IDT-DNA	unlabeled 5′ – CTTTGCTCA GGTCCACCGG – 3′; RRID: NA
Recombinant DNA		
RP23-329L1 unmodified BAC	CHORI	RRID: NA
RP23-181A2 unmodified BAC	CHORI	RRID: NA
RP24-68J22 unmodified BAC	CHORI	RRID: NA
RP23-307B16 unmodified BAC	CHORI	RRID: NA
RP23-199D5 unmodified BAC	CHORI	RRID: NA
RP24-344N1 unmodified BAC	CHORI	RRID: NA
RP23-126C5 unmodified BAC	CHORI	RRID: NA
RP23-329L1 - eGFP-L10a	This paper	Cacng5-bacTRAP - modified BAC; RRID: NA
RP23-181A2 - eGFP-L10a	This paper	Calca-bacTRAP - modified BAC; RRID: NA
RP24-68J22- eGFP-L10a	This paper	Cartpt - modified BAC; RRID: NA
RP23-307B16 - eGFP-L10a	This paper	Sh3bgrl2-bacTRAP - modified BAC; RRID: NA
RP23-199D5 - eGFP-L10a	This paper	Rasgrp2-199D5-bacTRAP - modified BAC; RRID: NA
RP24-344N1 - eGFP-L10a	This paper	Rasgrp2-344N1-bacTRAP – modified BAC; RRID: NA
RP23-126C5 - eGFP-L10a	This paper	Sstr4-bacTRAP - modified BAC; RRID: NA
mouse Ptbp1 untagged cDNA clone NM_008956	Origene	Cat# MG223224; RRID: NA
Software and Algorithms		
htseq	Anders et al., 2015	https://github.com/htseq/htseq
FIMO	Grant et al., 2011	http://meme-suite.org/doc/fimo.html
edgeR	Robinson et al., 2010	http://bioconductor.org/packages/devel/bioc/html/edgeR.html

(*Continued on next page*)

Neuron
NeuroResource

CellPress

Continued

REAGENT or RESOURCE	SOURCE	IDENTIFIER
The Sleipnir Library for Computational Functional Genomics	Huttenhower et al., 2008	https://libsleipnir.bitbucket.io/
VEGAS2	Mishra and Macgregor, 2015	https://vegas2.qimrberghofer.edu.au/
STAR	Dobin et al., 2013	https://github.com/alexdobin/STAR

RESOURCE AVAILABILITY

Lead Contact
Further information should be directed to and will be fulfilled by the Lead Contact, Olga Troyanskaya (ogt@cs.princeton.edu).
   Specific questions regarding experimental details and reagents should be directed to Jean-Pierre Roussarie (jroussarie@rockefeller.edu).

Materials Availability
All modified BACs and embryos for some of the bacTRAP mice generated in this study (Sh3bgrl2-, Rasgrp2-, Sstr4#7-, Sstr4#19-, and Calca- are frozen at Rockefeller University and available on request). For the other bacTRAP mice generated in this study, transgene expression was lost across generations, as is often the case with BAC transgenic lines, and the lines were discontinued. The materials are available from corresponding author Jean-Pierre Roussarie (jroussarie@rockefeller.edu) with a completed Materials Transfer Agreement.

Data and Code Availability
- The datasets generated during this study are available at GEO: GSE151460 for the bacTRAP profiles at 5, 12, and 24 months of age and the APP/PS1 ECII-bacTRAP profiles, and GSE151356 for the ECII-bacTRAP data upon silencing and overexpression of Ptbp1.
- The Sleipnir library for functional genomics used for network integration is available at https://libsleipnir.bitbucket.io/.
- Uncropped original images for western blot and fluorescent PCR for Figures 5 and S3 in the paper are available have been deposited to Mendeley Data: https://dx.doi.org/10.17632/g67bhh7zsj.1.

EXPERIMENTAL MODEL AND SUBJECT DETAILS

In vivo animal studies
All experiments were approved by the Rockefeller University Institutional Animal Care and Use Committee (RU-IACUC protocols #07057, 10053, 13645-H, 16902), and were performed in accordance with the guidelines described in the US National Institutes of Health Guide for the Care and Use of Laboratory Animals. Mice were housed in groups of up to 5 animals on a 12 h dark/light cycle at 22°C and provided with rodent diet (Picolab) and water *ad libitum*. All animals were drug and test naive (other than genotyping) when they were used for the described experiment. Littermates of the same sex were randomly assigned to the different groups. All bacTRAP mice and APP/PS1 mice (B6.Cg-Tg(APPswe,PSEN1dE9)85Dbo/Mmjax purchased from the Jackson laboratories) were maintained in a heterozygous state by crossing them with non-transgenic C57BL/6J mice (Jackson Lab). Human tau phage artificial chromosome (PAC) mice (B6.Cg-*Mapt*$^{tm1(EGFP)Klt}$ Tg(MAPT)8cPdav/J purchased from the Jackson lab) express the full wild-type human MAPT gene transgenically, as part of a phage artificial chromosome (Andorfer et al., 2003). In these mice, both 3R and 4R human tau isoforms are present in adult neurons, while in wild-type mice, adult neurons express only 4R mouse tau. Htau PAC mice were maintained by crossing (htau PAC +/− , mtau KO/KO) with wild-type C57BL/6J mice. For cell-type specific profiling in wild-type mice, only male mice were used, and the tissue from two males was pooled. Each type of neuron was profiled at 4-5 months, 12 months, and 24 months. For comparing ECII neurons in wild-type and APP/PS1 mice, both male and female mice were used, and each sample corresponded to the tissue of one mouse. (see Table S7 for genotyping primers). Baseline PTB expression was tested in 3-month old C57BL/6J mice. Stereotaxic injections were performed in 8 to 11 month-old female and male (htau PAC +/−, mtau KO/+) mice.

Mouse genotyping
All mice were genotyped by PCR on tail clips using the following primers: GFP-forward 5′-GACGTAAACGGCCACAAGTTCAG-3′ and GFP-reverse 5′-ATGGTGCGCTCCTGGACGTAG-3′ for all bacTRAP mice and for htauPAC mice (testing for the presence of the mouse tau knockout allele), APP-forward 5′-AGGACTGACCACTCGACCAG-3′, APP-reverse 5′-CGGGGGTCTAGTTCTGCAT-3′, PSEN1-forward 5′-AATAGAGAACGGCAGGAGCA-3′ and PSEN1-reverse 5′-GCCATGAGGGCACTAATCAT-3′ for APP/PS1 mice, and htau-forward 5′-ACTTTGAACCAGGATGGCTGAGCCC-3′, htau-reverse 5′-CTGTGCATGGCTGTCCACTAACCTT-3′ (testing for the presence of the human tau PAC allele), mtau-forward 5′- CTCAGCATCCCACCTGTAAC

−3′, mtau-reverse 5′-CCAGTTGTGTATGTCCACCC-3′ (testing for the presence of the endogenous mouse tau allele) (Andorfer et al., 2003).

Cell culture

The SH-SY5Y neuroblastoma cell line were purchased from ATCC (sex: female), and used directly after purchase. It was grown in DMEM/F-12 medium supplemented with 10% fetal bovine serum, at 37°C in 5% CO_2. For mouse entorhinal cortex neuron primary cultures, we used timed pregnant C57BL/6J female mice (Jackson laboratory) at E17 in utero. Briefly, entorhinal cortices from embryos were dissected and incubated at 37°C in 0.05% Tripsine/EDTA (Life Technologies, USA) for 10 min. After centrifugation the tissue pellet was dissociated in HBSS containing 0.5mg/ml DNase I (Roche) with a Pasteur pipette. Cells were seeded at 25,000 cells/cm^2 in Neurobasal media (Thermo Fisher) with 2% B-27 supplement (Thermo Fisher) and 2 mM GlutaMAX (Thermo Fisher), and incubated at 37 °C in a humidified 5% CO_2-containing atmosphere. Neuron treatments were performed after a minimum of 10 days in vitro day.

METHOD DETAILS

bacTRAP transgene construction

To construct cell type-specific bacTRAP mice, we searched for drivers specific to each type of neuron. For that purpose, we mined the ABA and GENSAT databases for genes expressed selectively in the different cell types of interest. We selected the following genes: Rasgrp2 and Sh3bgrl2 (Reln-expressing ECII principal neurons), Sstr4 (CA1 pyramidal neurons), Cacng5 (CA2 pyramidal neurons), Gprin3 (CA3 pyramidal neurons), Calca (V1 pyramidal neurons), Cartpt (S1 pyramidal neurons) for enriched expression in the cell type of interest compared to neighboring cell types. Regulatory regions of these genes should drive expression in the corresponding neuron types. We thus used these genes to construct corresponding bacTRAP mice according to previously described procedures (Gong et al., 2003). Specifically, we obtained the bacterial artificial chromosomes (BACs) where the open reading frame (ORF) for each of these genes is most centrally located, ensuring that both upstream and downstream regulatory sequences are driving the expression of the bacTRAP construct: RP23-307B16 (Sh3bgrl2), RP23-199D5 and RP24-344N1 (Rasgrp2), RP23-126C5 (Sstr4str), RP23-329L1 (Cacng5), RP23-181A2 (Calca), RP24-68J22 (Cartpt) (Children's Hospital and Research Center at Oakland, CHORI). We then set out to modify each BAC to place the eGFP-L10a cDNA under the control of each gene's regulatory sequences (Gong et al., 2003). For each gene, we first amplified by PCR on the non-modified BAC a small homology arm corresponding to approximately 500 bp of sequence upstream of the gene ORF, stopping 5 bp before the ORF (sequences of all small homology arms in the Table S7), and cloned it in the S296 shuttle vector (a pLD53.SC2 plasmid containing the cDNA for eGFP-L10a). Integration of eGFP-L10a in the BACs takes place when the non-modified BAC, the corresponding shuttle vector carrying the small homology arm upstream of eGFP-L10a, and the recA recombinase are co-expressed in the same bacteria. For that purpose, we first made the BAC host cells competent for transformation: BAC host cells obtained from CHORI were grown overnight at 37°C with chloramphenicol (20 μg/ml). A single colony was then grown for each BAC to an optical density of 0.8 in chloramphenicol. Cells were harvested by centrifugation, resuspended in an ice-cold solution of 50 mM $CaCl_2$ and kept on ice for 15 minutes. Cells were then pelleted again and resuspended in an ice-cold solution of 50 mM $CaCl_2$ and 20% glycerol before being snap-frozen. Competent BAC host cells were then chemically transformed with PSV1.recA plasmid coding for recA and grown overnight at 30°C with chloramphenicol and tetracycline (10 μg/ml) to an optical density of 0.8. Cells were then made electro-competent by pelleting them, resuspending them in 10% glycerol, washing them twice in 10% glycerol and snap freezing them. Lastly each type of BAC-recA competent cells was electroporated with the S296 vector containing the corresponding small homology arm. Cells were then grown overnight at 30°C on chloramphenicol, tetracycline and ampicillin (50 μg/ml) to allow for BAC recombination. Cells were then grown overnight on chloramphenicol and ampicillin plates at 43°C, to select for cells with co-integrate BAC clones. Co-integrates were first screened by PCR on individual colonies. The proper integration of eGFP-L10a at the beginning of each ORF was monitored using Southern blot on the colonies that came positive from PCR screening. Purified BAC stocks were prepared using $CsCl_2$ gradient and BACs were linearized with PI-SceI before injection. Linearized BACs were dialyzed on 0.025 μm filter membranes (Millipore). Their quality and concentration was assessed on a pulse-field gel. The Rockefeller University Transgenic Services then performed pronuclear injection of the linearized BACs in fertilized oocytes of C57BL/6J mice (Jackson Lab). BacTRAP mice were crossed at all subsequent generations with C57BL/6J mice. F1 and F2 of the different founder lines were then tested for proper expression pattern. One of the founder lines with the Sstr4 BAC (Sstr4#19 line) presented ectopic expression in granule cells from the dentate gyrus and no expression in CA1 neurons. We thus used Sstr4#19 for granule cell profiling. We used another founder line (Sstr4#7) for CA1 neurons. We also separately obtained Cck- and Gprin3-bacTRAP mice, which were previously described (Doyle et al., 2008; Gray et al., 2018).

Detail of the bacTRAP mice analyzed

Table S7 lists the bacTRAP lines used for each of the different cell types.

Cell type-specific molecular profiling

To isolate cell type-specific mRNA, bacTRAP mice from the different transgenic lines were decapitated after slight CO_2 intoxication, and brains were promptly taken out. For each transgenic line, we dissected the minimal area where transgene expression is restricted

CellPress

to the cell type of interest (for ECII bacTRAP lines, we made a coronal cut around −3.3 mm anteroposterior (AP); for Sh3bgrl2-bac-TRAP, we then scooped the hippocampus off the tissue caudal to the cut, discarded it, and kept the tissue located ventral to the rhinal fissure; for Rasgrp2-bacTRAP, we took all the tissue caudal to the −3.3 mm AP cut, and ventral to a horizontal cut around −3 mm dorsoventral (DV); for Sstr4#7- and Sstr4#19-bacTRAP lines, we used all the hippocampus; for the Cck-, Cacng5- and Gprin3-bac-TRAP lines, we used all the hippocampus rostral from a coronal cut around −3.3mm AP; for Calca-bacTRAP, we made a sagittal cut around +3.6 mm mediolateral (ML) on each side, a coronal cut around −3 mm AP and we extracted the cortex respectively dorsal and caudal to these cuts, while cutting out the mEC; for Cartpt-bacTRAP we made coronal cuts around 1.75 mm AP, −0.25 mm AP, and −2.25 mm AP and for each slice, we dissected out the part of the cortex that contains the somatosensory cortex).

We then performed bacTRAP purification following the previously described procedure (Heiman et al., 2008) except for two differences. First the volume of lysis buffer used for tissue homogenization depends on the size of each particular brain region. The buffer volumes for each bacTRAP line are shown in Table S7. Second, we used RNeasy Plus Micro Kit (QIAGEN) to purify RNA after bacTRAP, and RNA was thus detached from beads using the RLT Plus buffer supplemented with 1% β-mercaptoethanol (MP biomedicals). RNA integrity was evaluated with a bioanalyzer RNA 6000 pico chip (Agilent) and RNA quantified by fluorescence detection with Quant-It Ribogreen RNA reagent (ThermoFisher). All samples included in the study had RNA Integrity Numbers above 7. Five ng of RNA were then used for reverse-transcription with Ovation RNaseq v2 kit (NuGEN). cDNAs were cleaned up using a QIAquick PCR purification kit (QIAGEN). Double-stranded cDNAs were quantified by fluorescence detection using Quant-IT Picogreen dsDNA reagent (ThermoFisher). cDNAs (200 ng) were sonicated in 120 μL volume using a Covaris S2 ultrasonicator (duty cycle, 10%; intensity, 5; cycles/burst, 100; time, 5 minutes) to generate 200 bp fragments on average. The fragmented cDNAs were then used to construct sequencing libraries using TruSeq RNA sample prep kit v2 (Illumina). Library concentration was evaluated using bioanalyzer, and libraries were multiplexed. Multiplexes were then sequenced at the Rockefeller University genomics resource center with a HiSeq 2500 sequencer (Illumina).

Histology

To study the expression pattern of the bacTRAP transgene, bacTRAP mice were transcardially perfused with 4% paraformaldehyde. Dissected brains were fixed by immersion for one hour in 4% paraformaldehyde, frozen embedded in OCT compound (TissueTek), and cut in 40 μm-thick sections on a CM3050 S cryostat (Leica). Sections were permeabilized in PBS with 0.1% Fish Gelatin (Sigma), 2% normal goat serum (Jackson ImmunoResearch), and 0.1% Triton X-100 and then stained overnight at 4°C in PBS with 0.1% fish gelatin and 2% normal goat serum with a chicken anti-GFP antibody (1/300). The primary antibody was detected with an Alexa 488-donkey anti-chicken secondary antibody (1/300). After the last wash, sections were mounted with Prolong Gold Medium containing DAPI. Sections were imaged using a Zeiss LSM 510 META laser scanning confocal microscope. Images were minimally processed using Photoshop (Adobe Systems) to enhance brightness and contrast for optimal representation of the data.

Comparison of the bacTRAP profiles with Allen Brain Atlas

In order to cross-validate the bacTRAP profiles, we compared them to Allen Brain Atlas *in situ* hybridization (ISH) pictures. Based on cell type-specific bacTRAP data, we first calculated an ontology z-score for each gene in each neuron type. For each neuron type, we obtained the 50 genes with the highest ontology z-scores. We then analyzed coronal - whenever possible - or sagittal ISH sections from the Allen Brain Atlas, for each of these genes (50 genes per 7 types of neuron). We scored expression in the seven types of neuron using the Allen Brain Atlas "expression" tool, blind to the identity of the gene, and to the region where it is enriched. Similarly to what Cembrowski et al. (2016) had done to cross-validate their data, we verified that each gene predicted to be enriched in a given neuron type with our bacTRAP data indeed presented expression in the corresponding neuron type in the Allen Brain Atlas (ABA). We found excellent correspondence between our data and the ABA data, as 98%, 100%, 96%, 100%, 98%, 94% and 87% of the genes predicted to be enriched in ECII, CA1, CA2, CA3, DG, S1 and V1 neurons respectively indeed showed expression in the correct regions in the ABA (we disregarded genes that do not show expression in any ISH section that are probably expressed below the detection level). In addition, we show detectable signal in our bacTRAP data for some genes with no ABA ISH signal, like Pkib for example. ISH pictures for the five genes with the highest ontology z-scores for each neuron type, that were available on the ABA, and that showed expression in some parts of the brain, are shown in Figure S1. The reference for the ABA Images shown on Figure 2 and on Figure S1 are the following: *for Figure 2:* Reln (Image series: 890, image: 135, http://mouse.brain-map.org/experiment/show/890), Lamp5 (70927827, 313, http://mouse.brain-map.org/experiment/show/70927827), Whrn (77371813, 168, http://mouse.brain-map.org/experiment/show/77371813), Wfs1 (74881161, 260, http://mouse.brain-map.org/experiment/show/74881161), Ptpn5 (74743293, 253, http://mouse.brain-map.org/experiment/show/74743293), Bok, (71064032, 252, http://mouse.brain-map.org/experiment/show/71064032), Prox1 (73520980, 237, http://mouse.brain-map.org/experiment/show/73520980); *for Figure S1:* Nr2f2 (308055507, 9, http://mouse.brain-map.org/experiment/show/308055507), Apaf1 (68745275, 8, http://mouse.brain-map.org/experiment/show/68745275), Camk2d (68668030, 5, http://mouse.brain-map.org/experiment/show/68668030), Reln (79394359, 13, http://mouse.brain-map.org/experiment/show/79394359), Rab3c (69816745, 13, http://mouse.brain-map.org/experiment/show/69816745), Rasd1 (2521, 219, http://mouse.brain-map.org/experiment/show/2521), Neurod6 (698, 224, http://mouse.brain-map.org/experiment/show/698), Arhgap12 (71836846, 258, http://mouse.brain-map.org/experiment/show/71836846), Kcnab2 (1754, 221, http://mouse.brain-map.org/experiment/show/1754), Hpca (72129291, 248, http://mouse.brain-map.org/experiment/show/72129291), Fam19a5 (69059974, 97, http://mouse.brain-map.org/experiment/show/69059974), Prkca (77869816, 268, http://mouse.brain-map.org/experiment/show/77869816), Scrg1 (71924331, 268, http://mouse.brain-map.org/experiment/show/71924331), Syce2 (70609150, 74, http://mouse.brain-map.org/experiment/show/

70609150), Nrip3 (73520999, 270, http://mouse.brain-map.org/experiment/show/73520999), Ociad2 (75041527, 269, http://mouse.brain-map.org/experiment/show/75041527), Rnf182 (70719034, 92, http://mouse.brain-map.org/experiment/show/70719034), Mpped2 (73497744, 74, http://mouse.brain-map.org/experiment/show/73497744), Prox1 (73520980, 237, http://mouse.brain-map.org/experiment/show/73520980), Synpr (1862, 229, http://mouse.brain-map.org/experiment/show/1862), Lhfpl2 (72007934, 258, http://mouse.brain-map.org/experiment/show/72007934), Slc39a6 (73930852, 246, http://mouse.brain-map.org/experiment/show/73930852), Smad3 (70593360, 72, http://mouse.brain-map.org/experiment/show/70593360), Kcnh5 (77620826, 61, http://mouse.brain-map.org/experiment/show/77620826), Rorb (79556597, 161, http://mouse.brain-map.org/experiment/show/79556597), Pak7 (75988567, 165, http://mouse.brain-map.org/experiment/show/75988567), Sytl2 (73520979, 316, http://mouse.brain-map.org/experiment/show/73520979), Rspo1 (73636101, 152, http://mouse.brain-map.org/experiment/show/73636101), Lamp5 (70927827, 313, http://mouse.brain-map.org/experiment/show/70927827), Cbln2 (70231306, 300, http://mouse.brain-map.org/experiment/show/70231306), Tbc1d30 (72283432, 1, http://mouse.brain-map.org/experiment/show/72283432), Kalrn (73930821, 302, http://mouse.brain-map.org/experiment/show/73930821).

Cell culture

For siRNA experiments, cells were seeded at a density of 4×10^5 cells per well in 12-well plates and treated the following day with 1 μM of Accel siRNA (Dharmacon) – either non-targeting control pool or PTBP1 directed SMARTpool. We harvested cells three days after treatment with PureLink Mini Lysis buffer supplemented with β-mercaptoethanol. The first column flow-through from the PureLink Mini kit was precipitated with acetone for protein analysis. For RNA-sequencing, RNA was purified from the column-bound material following the manufacturer's instructions, with an in-column DNase digestion (QIAGEN RNase-free DNase set). The resulting RNA was quantified using a Nanodrop One. Sequencing libraries were synthesized using 400 ng of RNA and an Illumina TruSeq RNA sample prep kit v2. Library concentration was evaluated using high-sensitivity DNA tapestation (Agilent), and libraries were multiplexed. Multiplexes were then sequenced at the Rockefeller University genomics resource center with a NextSeq sequencer and 75 bp paired-end reads (Illumina). Libraries from five independent samples were sequenced for each condition. For verifying the successful downregulation of PTBP1, we probed proteins from the same cells by western blot. We cleaned up the acetone precipitates obtained above with ice-cold ethanol, resuspended the precipitates in RIPA supplemented with Complete mini protease inhibitors (Roche), and sonicated them to resuspend them properly.

Protein and RNA extraction from brain lysates

For extracting bulk protein and RNA from the mouse brain, brains were dissected out, and EC, neocortex, hippocampus and spleen were snap frozen. For investigating Ptb protein expression, tissue was sonicated for 1 minute in ice-cold RIPA buffer supplemented with complete protease inhibitors. For investigating both protein and RNA contents in mice stereotaxically injected with control or Ptb viruses, the EC was homogenized mechanically in a small volume of PBS 1X supplemented with complete mini protease inhibitors (Roche), Phos-STOP phosphatase inhibitors (Roche), RNasin (40 U/ml) and Superasin (20 U/ml), using a motorized homogenizer. Part of the homogenate was then used for RNA extraction, and part for protein. For the RNA fraction, Purelink RNA mini lysis buffer was added to the homogenate and RNA was purified following the manufacturer's instructions. For the protein fraction, ice-cold RIPA buffer supplemented with protein and phosphatase inhibitors was added. The protein extracts were then centrifuged for 10 minutes at 10,000 g to pellet insoluble debris.

Tau splicing analysis

For studying tau splicing on bulk EC lysates, or on SH-SY5Y lysates, RNA was quantified using a nanodrop. RNA (500 ng) was reverse-transcribed for these samples, using Superscript III first strand synthesis system (ThermoFisher) with a 1:1 mix of oligo-dT primers and random hexamers from the kit. RNA was degraded using RNase H after reverse-transcription. qPCR was then run on these cDNA using TaqMan Universal PCR mastermix and the following FAM-labeled TaqMan assays in a Life Technologies QuantStudio 12K-flex machine: Human GAPDH endogenous control, Hs00240906_m1 (human α-synuclein), Hs00902193_m1 (total human tau - primers and probe spanning exon 11 and 12), Hs00902312_m1 (exon 10-containing human tau – primers and probe spanning exon 9 and exon 10), Hs00902192 (non-exon-10-containing human tau – primers and probe spanning exon 9 and exon 11). Hs00738538 (human PTBP1), mouse GAPDH endogenous control, Mm01731480 (mouse Ptbp1). Ct values were analyzed with default settings in the Quantstudio software. For testing tau splicing with fluorescent PCR, we ran a regular PCR on carefully titrated cDNA amounts and PCR cycle numbers to ensure linear amplification range, following previously published methods (Andorfer et al., 2003; Furlanis et al., 2019; Wamsley et al., 2018), using the following HPLC-purified primers (designed by Duff et al., 2000): for human tau, forward primer: 5′-IRDye 800 – CTCCAAAATCAGGGGATCGC – 3′, reverse primer: unlabeled 5′ – CCTTGCTCAGGT CAACTGGT – 3′ (IDT-DNA), for mouse tau, forward primer: 5′-IRDye 800 – CACCAAAATCCGGAGAACGA – 3′, reverse primer: unlabeled 5′ – CTTTGCTCAGGTCCACCGG – 3′. For both human and mouse tau, the PCR amplifies a 297-nucleotide band from 3R-tau, and a 390-nucleotide band from 4R-tau. Labeled PCR products were then loaded on a 1 mm Novex TBE 10% polyacrylamide gel. The 1 kb plus DNA ladder was stained with SYTO 60 for evaluating fragment size. The gels were imaged with a Li-COR Odyssey with an offset of 0.5 mm and quantified in the Odyssey software.

Western blot

For verifying Ptbp1 knockdown, protein concentrations were determined using a BCA assay. Ten μg of protein were denatured at 85°C for 3 minutes and loaded in a 4%–12% Bis-Tris gel in MOPS buffer. The gel was transferred to nitrocellulose membranes. Mem-

branes were blocked for 1 h in Li-COR blocking buffer, incubated overnight with goat anti-PTBP1 (ab5642, Abcam, 1/1,500) and mouse anti-actin (8H10D10, Cell Signaling, 1/1,000) primary antibodies diluted in Li-COR blocking buffer supplemented with 0.1% of Tween-20, and incubated for 1 h in secondary antibody (donkey anti-goat IRDye 680 antibody, donkey anti-mouse IRDye 800) in TBS-Tween. Blots were imaged using a Li-COR Odyssey.

Stereotaxic injections

Purified Adeno-associated virus (AAV1 subtype) obtained from Vector Biolabs were injected in the EC of adult mice using an Angle Two mouse stereotaxic frame with a motorized nanoinjector (Leica). Animals were anesthetized with xylazine (4.5 mg/kg body weight) and ketamine (90 mg/kg body weight) injected peritoneally. An ophthalmic ointment was applied to the anesthetized animals to prevent corneal drying during the procedure. AAVs were loaded in a 10 μL syringe (Hamilton, 7653-01) with a 33-gauge needle (Hamilton, 7803-05). 2×10^{13} genome copies of AAV1 particles were injected in 2 μl, in the mouse EC (AP: −3.70; ML: −4.65; DV: −4.50) with the nanoinjector tilted −4.05°. The contralateral EC (AP: −3.70; ML: +4.65; DV: −4.50) was injected with a nanoinjector tilt of +4.05°. Injection rate was 0.4 ml/min. For testing the effects of Ptb silencing or overexpression in ECII neurons specifically, ECII-bacTRAP mice (Sh3bgrl2-bacTRAP) were injected (the same virus was injected on both sides). The viruses used for Ptb silencing were the following: AAV1-mCherry-U6-mPTBP1-shRNA (carrying a small hairpin RNA (shRNA directed against Ptb under the control of a U6 promoter, shRNA sequence: *5′-CCGG-CTCAATGTCAAGTACAACAATCTCGAGATTGTTGTACTTGACATTGAG-TTTTT −3′*) and AAV1-mCherry-U6-scrmb-shRNA (control for the Ptb silencing virus, shRNA sequence: *5′-CCGG-CAACAAGATGAAGAGCACCAA-CTCGAG-TTGGTGCTCTTCATCTTGTTG-TTTTT-3′*).

The viruses used for overexpression were the following: AAV1-hSyn1-mCherry-WPRE (empty control expressing mCherry under the control of the human synapsin-1) and AAV1-hSyn1-mPTBP1-IRES-mCherry (expressing the cDNA encoding mouse Ptb Δexon 9 isoform, under the control of the human synapsin-1 promoter, NM_008956 from Origene, and mCherry). For testing tau splicing *in vivo*, AAV1-hSyn1-mPTBP1-IRES-mCherry and AAV1-hSyn1-mPTBP1-IRES-mCherry were injected contralaterally. To avoid side-specific bias, test and control viruses were injected in alternating sides. Bacitracin antibiotic gel was applied to the surgery wound, that was sutured with a non-absorbable monofilament. Warm, sterile saline solution was injected intraperitoneally (3% of the body weigh) to compensate fluid loss, and animals were monitored until complete recover from anesthesia. Mice were sacrificed for RNA and protein isolation 1 to 2 weeks after virus injections. For all injections, we tested the presence of mCherry by qPCR. We excluded 1 bacTRAP mouse in the Ptbp1 silencing experiment, and 1 bacTRAP mouse in the Ptb overexpression experiment, which did not have mCherry expression in the EC.

RNA-seq analysis

RNA-sequencing reads were mapped to the mouse genome (Ensembl 75) using STAR (version 2.3.0e, default parameters) (Dobin et al., 2013), and gene-level counts were quantified using htseq-count (version 0.9.1) (Anders et al., 2015). Genes were subjected to an expression detection threshold of 1 count per million reads per gene in more than 3 samples and oligodendrocyte, endothelial, and ependymal cell gene clusters were excluded to focus on the neuronal signal. These clusters were identified by constructing co-expression matrices, and the gene clusters with canonical oligodendrocyte, endothelial, and ependymal cell genes (olig: Olig1 (OPC), Mag (mature oligos); epend: Foxj1, Sntn; endot: Kdr, Vwf, Tek (pericytes)) were excluded. Differential expression and multidimensional scaling analysis were performed using edgeR (version 3.8.6) (Robinson et al., 2010).

Spatial homology analysis

Human brain microarray data were downloaded from the ABA (http://human.brain-map.org/static/download) (Hawrylycz et al., 2012). Brain regions that were measured in fewer than 3 out of the 6 subjects profiled were excluded from downstream analysis to ensure robustness.

We calculated an ontology-aware spatial homology score between each of our 7 mouse neuron types and each of the 205 human brain regions robustly measured by the ABA, as follows:

$$\psi_{ij} = \left(\sum_{g \in S_i} \frac{\alpha_{jg}^{(h)}}{\#\{g \in S_i\}} \right), j = 1, \ldots, T_m, j = 1, \ldots, T_h,$$ for mouse neuron type i and human brain region j (thus $T_m = 7$ and $T_h = 205$), human gene g.

$$S_i = \left\{ g \,\middle|\, \alpha_{ig}^{(m)} > \frac{1}{T_m} \sum_{i=1}^{T_m} \text{quantile}\left(\overrightarrow{\alpha}_i^{(m)}, q\right) \right\} \cap \left\{ g \,\middle|\, \mu_{ig} > \frac{1}{T_m} \sum_{i=1}^{T_m} \text{quantile}\left(\overrightarrow{\mu}_i, q\right) \right\}, \quad \alpha_{jg}^{(h)} = \frac{\mu_{jg} - \mu'_{jg}}{\sqrt{\frac{\sigma_{jg}^2}{N_j} + \frac{\sigma_{jg}'^2}{N_j'}}}, \quad \alpha_{ig}^{(m)} = \frac{\mu_{ig} - \mu'_{ig}}{\sqrt{\frac{\sigma_{ig}^2}{N_i} + \frac{\sigma_{ig}'^2}{N_i'}}}$$

where μ_{ig}, σ_{ig} are respectively the mean and standard deviation of expression for the closest mouse functional ortholog (Park et al., 2013) of gene g in mouse neuron type i (in log$_2$(rpkm)), while μ'_{ig}, σ'_{ig} are the mean and standard deviation of expression values for the mouse ortholog for unrelated neuron types (e.g., for neuron type hippocampus CA2, μ'_{ig} would be the mean expression of all non-hippocampus neuron types). N_i is the number of samples for neuron type T_i. The quantile used was $q = 0.9$. Normalized microarray expression values as processed by the Allen Institute of Brain Science were used to calculate the corresponding scores (μ_{jg}, σ_{jg}, etc.) for gene g in human. Intuitively, $\alpha_{ig}^{(m)}$ is a normalized enrichment score for the mouse ortholog of gene g in neuron type T_i of the mouse. S_i is the set of genes that

are both highly expressed (high μ_{ig}) and highly specific (high $\alpha_{ig}^{(m)}$) to tissue T_i, thus providing a strong molecular signature for that tissue. This signature is combined with the enrichment scores from human ($\alpha_{jg}^{(h)}$) to produce a final spatial homology score.

To provide a quantitative summary for the spatial homology mapping, we also calculated a mouse-human tissue match score $\bar{\nu} = \left(\sum_{i=1}^{T_m} \frac{\nu_i}{T_m}\right)$, the average of individual match scores per mouse neuron type, $\nu_i = \max_{p \in M_i}\left\{T_h - \frac{r_{ip}}{T_h}\right\}$, where

$$M_i = \left\{t \mid t \in \mathrm{match}^{(h)}(i)\right\}, \; r_{ip} = \#\left\{j \mid \psi_{ij} > \psi_{ip}\right\} + \frac{\#\left\{j \mid \psi_{ij} = \psi_{ip}\right\} - 1}{2}.$$

Briefly, for mouse neuron type i, M_i is the set of 'perfect' human brain region matches based on anatomy (Table S2), and r_{ip} is the rank (in the event of ties, i.e., identical spatial homology scores, the mean of the tied ranks is used) of human brain region p for mouse neuron i among all possible human brain regions (1 corresponds to the best ranked, and $T_h = 205$ is the worst ranked). To facilitate comparisons, we transform the simple rank score to be between 0 and 1, where 1 corresponds to the best rank. When there are multiple human brain regions that match to the same mouse neuron type (e.g., ECII neurons are located in the human parahippocampal gyrus, and the Allen Brain Atlas had data for both parahippocampal gyrus, bank of the collateral sulcus, as well as parahippocampal gyrus, lateral bank of gyrus), the maximum transformed rank score was taken as the individual match score (ν_i).

To evaluate the spatial homology mappings, we permuted the spatial homology scores to create a null distribution of mouse-human tissue match scores (n = 10,000) and found that the spatial homology mapping was highly significant (p value < 0.0001). To examine how sensitive the homology mapping was to the choice of quantile threshold, we varied the quantile threshold from 0.1 to 0.97 (q = 0.97 was the highest for which all mouse neuron types still had expression signatures that passed the threshold). Permutation tests at each threshold (n = 1,000) showed that the spatial homology mapping was significantly better than random for thresholds at higher than q = 0.4 and that the mappings stabilized after q = 0.7 (Figure S2A).

Construction of functional networks

We used the cell type-specific molecular signatures to construct a cell-type specific gold standard (see Gold standard section below), which we then used to integrate a human genome-scale data compendium (see Human data compendium section below) to construct cell-type specific functional networks based on our tissue-specific regularized Bayesian integration method (Greene et al., 2015) (see Data integration section below).

Gold standard

The cell-type-specific gold standard was constructed by combining a functional interaction standard and cell-type-specific signatures. The functional interaction gold standard was constructed based on either the presence or absence of gene co-annotations to expert-selected biological process terms from the Gene Ontology (GO), based on whether the term could be experimentally verifiable through targeted molecular experiments. For each of these 337 selected GO terms, we obtained all experimentally derived gene annotations (i.e., annotations with GO evidence codes: EXP, IDA, IPI, IMP, IGI, IEP). After gene propagation in the GO hierarchy, gene pairs co-annotated to any of the selected terms were considered positive examples, whereas gene pairs lacking co-annotation to any term were considered negative examples, except in cases where the two genes were (i) separately annotated to highly overlapping GO terms (hypergeometric p value < 0.05) or (ii) co-annotated to higher-level GO terms that may still indicate the possible presence of a functional relationship.

We then combined our expanded cell-type-specific molecular gene signature sets (q = 0.75) with this functional interaction standard by defining the four classes of edges (C1, C2, C3, and C4) as described in Greene et al. (2015), with the adjustment of allowing genes annotated to nervous system tissues to be considered for the C2 negative example class (to emphasize cell-type specificity in relation to other general nervous system genes, rather than excluding them based on the hierarchical tissue ontology as in Greene et al., 2015). More specifically, for a neuron type i, C1 is the class of positive functional edges between genes that are also specifically coexpressed in i; C2 is the class of positive functional edges between a gene that is expressed in neuron type i and in an unrelated tissue or cell type (in our case, we consider general nervous system genes to also be in this class); C3 is the class of negative functional edges between genes that are coexpressed in neuron type i; C4 is the class of negative functional edges between one gene expressed in neuron type i and another gene specifically expressed in an unrelated tissue. C1 edges are considered positive examples (genes are both functionally related and expressed in the neuron type of interest), and C2-4 edges are negative examples (at least one of the conditions of functional relationship or tissue-specificity is violated).

Human data compendium

We downloaded and processed 31,157 human interaction measurements and brain expression-based profiles from over 24,000 publications, as well as experimentally defined transcription factor binding motifs, chemical and genetic perturbation data, and microRNA target profiles.

Physical interaction data were downloaded from BioGRID (version 3.2.118) (Chatr-Aryamontri et al., 2013; Stark et al., 2006), IntAct (Nov 2014) (Orchard et al., 2014), MINT (2013-03-26) (Licata et al., 2012), and MIPS (Nov 2014) (Mewes et al., 2011). Interaction edges from BioGRID were discretized into five bins (0-4), depending on the number of experiments supporting the interaction. For all other interaction databases, edges were discretized based on the presence or absence of an interaction.

A total of 6,907 expression profiles from 268 human brain expression datasets were downloaded from the Gene Expression Omnibus (GEO) (Barrett et al., 2013). Duplicate samples were collapsed, and genes with values missing in over 30% of the samples were removed. All other missing values were imputed (Troyanskaya et al., 2001). Normalized Fisher's z-transformed expression scores were calculated per pair of genes and discretized into the corresponding bin: $(-\infty, -1.5)$, $[-1.5, -0.5)$, $[-0.5, 0.5)$, $[0.5, 1.5)$, $[1.5, 2.5)$, $[2.5, 3.5)$, $[3.5, 4.5)$, $[4.5, \infty)$.

Experimentally defined transcription factor binding motifs were downloaded from JASPAR (Mathelier et al., 2014), and the 1-kb upstream region of each gene was scanned for presence of binding motifs using FIMO (Grant et al., 2011) from the MEME software suite (Bailey et al., 2015). For each pair of genes, the Fisher z-transformed Pearson correlation of binding profiles was calculated and discretized into one of the corresponding bins: $(-\infty, -1.5)$, $[-1.5, -0.5)$, $[-0.5, 0.5)$, $[0.5, 1.5)$, $[1.5, 2.5)$, $[2.5, 3.5)$, $[3.5, 4.5)$, $[4.5, \infty)$.

Chemical and genetic perturbation and microRNA target profiles were downloaded from the Molecular Signatures Database (MSigDB, c2:CGP and c3:MIR gene sets, respectively) (Subramanian et al., 2005). For each pair of genes, similarity based on the weighted mean of number of shared profiles (weighted by the specificity of the profile (1/len(genes)) was calculated and discretized into the corresponding bin: $(-\infty, -1.5)$, $[-1.5, -0.5)$, $[-0.5, 0.5)$, $[0.5, 1.5)$, $[1.5, 2.5)$, $[2.5, 3.5)$, $[3.5, 4.5)$, $[4.5, \infty)$.

Data integration
We applied our tissue-specific regularized Bayesian integration method (Greene et al., 2015) for each of the 7 neuron types to train a naive Bayesian classifier by comparing against the positive and negative examples from the cell-type-specific gold standard. For each cell type, we constructed a binary class node representing the indicator function for whether a pair of genes has a cell-type-specific functional relationship, conditioned on additional nodes representing each of the datasets in the data compendium. Each model was then applied to all pairs of genes in the data compendium to estimate the probability of tissue-specific functional interactions. All code for data integration is available in our open-source Sleipnir library for functional genomics (Huttenhower et al., 2008).

Network connectivity analysis
We calculated a z-score for cohesiveness of various biological process GO terms in each of the neuron-specific networks: $z_{cohesiveness} = \frac{X_{GO} - X_{null}}{SE_{null}}$, where X_{GO} is the mean posterior probability of all gene pairs within a particular GO term, and X_{null}, SE_{null} are respectively the mean and standard error of the null distribution (based on gene sets randomly sampled within all genes with a GO annotation, with equivalent size to the GO term in question).

NetWAS 2.0 on AD GWAS
Here, using an AD GWAS for Braak stages (NFT pathology-based staging) (Beecham et al., 2014) as gold standard and the ECII-specific functional network neighborhoods as features, we applied NetWAS 2.0 with n = 10,000 to rank each of the 23,950 genes for potential association to AD.

We trained support vector machine classifiers (Joachims, 2005) using (i) nominally significant (p value < 0.01) GWAS genes as positive examples, (ii) randomly sampled non-significant genes with probability proportional to their GWAS p value as negatives, and (iii) the network neighborhoods of genes as features. Thus, genes with lower p values (i.e., more significant) would have a lower chance of being chosen as a negative example than genes with higher p values. Gene-level p values were obtained using the versatile gene-based association study 2 (VEGAS2, version:16:09:002) software (Mishra and Macgregor, 2015).

To ensure robustness, we independently sampled *n* such sets of negatives and trained *n* support vector machines. After applying each of the support vector machines to re-rank genes, we aggregated the *n* rankings into a final NetWAS 2.0 gene ranking. Intuitively, the key advance of the NetWAS 2.0 method is that it leverages the GWAS p values as opposed to treating all non-significant genes as having equal probability of being negative examples as in the original NetWAS method (Greene et al., 2015).

Establishment of the expert-curated gene set
To establish amyloid and NFT gene sets, we recruited independent curators who were unaware of any of the NetWAS 2.0 results: a laboratory member who is an AD expert (doctoral degree in biology, 20 years of experience in the AD field), for the amyloid and NFT-1 gene sets, and separately, two professional curators (doctoral degrees in biology, combined 28 years of experience in curation of biomedical literature) for the NFT-2 gene set.

We asked the AD-expert curator to search for genes involved in tau phosphorylation, aggregation, cleavage, folding, localization, clearance (for the NFT-1 set), and in Aβ production, clearance, aggregation (for the amyloid set). The searches were done with PubMed, and included publications released between January 2000 and April 2017.

In order to build the NFT-2 gene list, the professional curators reviewed biological resources and the published literature for evidence of tau modification, which included tau phosphorylation, aggregation, cleavage, folding, localization, and clearance. tau association was not sufficient, rather a causal link for the modification was required. For example, proteins that affected tau modification when activated/inhibited/knocked-out/over produced or expressed in a mutant form were included on the gene list. Due to the requirement of a clear causal link, only low-throughput experiments carried out *in vitro* or *in vivo* were assessed whereas high-throughput studies were not considered. The main focus was on the modification of human tau, but relevant results shown in various cell lines and animal models were also evaluated. If the results were shown in any species other than human, then the corresponding human ortholog was added to the list. To avoid duplication of effort, multiple curated resources were initially explored for potential tau

modifiers present in different database download files from November, 2019. Custom download files for human tau were obtained from iPTMnet (Huang et al., 2018) to identify proteins responsible for tau phosphorylation/dephosphorylation. Only genes with experimental evidence were extracted and their associated PubMed references were verified. tau modifying gene products were also extracted from relevant Gene Ontology (GO) annotations created by the Alzheimer's Research United Kingdom — University College London (ARUK—UCL) team (Kramarz et al., 2018). Tau-related data already captured in BioGRID (Oughtred et al., 2019; Stark et al., 2006) was also examined by screening the biochemical activity class of interactions in which tau was the hit/prey protein. These interactions represent *in vitro* experiments in which a protein has been demonstrated to directly modify tau with post-translational modifications (PTMs) or via proteolytic processing. Additional Tau modifiers were added to the gene list based on a recently published review of the biological roles of the tau protein by Guo et al. (2017) and the original research articles cited in this review were further prioritized for curation. Curators then branched out to review the primary literature in more detail and include proteins with a more indirect Tau modifying role. To this end, online text-mining resources were used to triage the scientific literature, i.e., RLIMS-P (Torii et al., 2015) and PIE the search (Kim et al., 2012). RLIMS-P is an information retrieval and extraction tool that highlights text relevant to phosphorylation interactions and was used to triage papers using tau as the query gene. Curators also used PIE the search, which scores publications based on their likelihood of containing protein interaction data, by running queries containing the following tau modification terms: tau cleavage, tau aggregation, tau folding, Tau localization, or tau clearance. These searches resulted in lists of publications that were reviewed for evidence that the interaction had an effect on tau modification. All together, these curation efforts generated a list of 174 unique genes which were associated with their relevant tau modifications, UniProt protein accession IDs, and original references. Approximately 52% of the 174 unique genes on the tau modifier gene list were found using various literature searches or extracted from relevant reviews indicating this gene list could not be autogenerated from existing annotations found in various biological resources.

Analysis of NetWAS 2.0 predictions
Comparison against the ACT study
We downloaded paired RNA-seq trascriptomes and neuropathological quantifications from the ACT study (http://aging.brain-map.org/download/index; Miller et al., 2017). We then calculated, for every gene, the Fisher's z-transformed absolute Spearman's correlation between its expression in the hippocampus and its IHC amyloid plaque load across all samples.

To aggregate the scores without selecting an arbitrary cutoff, we calculated an amyloid plaque association score for each percentile cutoff averaging the transformed correlation scores for the top x% of NetWAS 2.0 genes (with x = 1%, 5%, 10%, 15%, ...,100%). We compared these scores against the counterparts calculated based on ranking by the p values in the Braak GWAS study. For the background distribution, we sampled an equivalent number of genes 1000 times per percentile cutoff.

To calculate bootstrapped 95% confidence intervals for the NetWAS 2.0 amyloid plaque association scores, we subsampled genes with replacement within each percentile cutoff.

Analysis of Liang et al. ECII dataset
We downloaded microarray expression profiles measuring LCM ECII neurons in control and AD patients (Liang et al., 2008). Data normalization and differential expression analysis were performed using limma (version 3.22.7) (Smyth, 2004). Genes with Benjamini-Hochberg multiple hypothesis test-corrected FDR $\leq$ 0.05 were considered significantly differentially expressed.

Identification of functional modules
To identify functional modules represented in our top NetWAS 2.0 genes, we created an ECII subnetwork using the top 10% (i.e., top 2,395) of NetWAS 2.0 ranked genes. Then, we used an approach based on shared k-nearest-neighbors (SKNN) and the Louvain community-finding algorithm (Blondel et al., 2008) to cluster the network into distinct modules. This approach alleviates the effect of high-degree genes and accentuates local network structure by connecting genes that are likely to be functionally clustered together in the ECII network. We calculated the ECII SKNN network by using the number of shared top k-nearest neighbors between genes as edge weights and taking the subnetwork defined by the top 5% of edge weights as the subnetwork for downstream analysis. The clustering presented here was calculated with k = 50, but we confirmed that the clustering was robust for k between 10 and 100. Enrichment of Gene Ontology biological process terms and of other experiment-derived gene sets of interest in each module were calculated using one-sided Fisher's exact tests, with Benjamini-Hochberg multiple hypothesis test correction to calculate FDR.

Gene connectivity analysis
For each gene g in each cell-type specific functional network, we calculated a z-score for gene connectivity, a measure of how central a gene is in the network:

$z_{\text{connectivity}} = \frac{\overline{x}_g - \mu}{\sigma/\sqrt{n}}$, where $\overline{x}_g$ is the average posterior probability of edges incident on gene g. μ, σ, and n are respectively the mean, standard deviation, and number of all edges in the network.

QUANTIFICATION AND STATISTICAL ANALYSIS

Statistical details for all experiments can be found in figure legends. The only samples excluded were: a) samples from two htau PAC misgenotyped mice in the Ptbp1 OE experiment (Figures 5D–5G), which were homozygous mouse tau knockout rather than heterozygous mouse tau knockout like all of the other mice of the experiment, b) samples from bacTRAP mice in the Ptbp1 silencing and Ptbp1 OE experiment which did not show any read mapping to mCherry in the RNaseq data, indicating that these samples did not

have any detectable presence of the transduction virus – one mouse in the Ptbp1 silencing experiment, one mouse in the Ptbp1 OE experiment (Figures S3E–S3G).

ADDITIONAL RESOURCES

We have made the following data available at http://alz.princeton.edu:

- Gene expression levels in the mouse across the 7 different types of neurons, at 5, 12 and 24 months of age ("Expression values").
- The seven *in silico* human genome-wide network models, each representing one AD-vulnerable or resistant neuron type in the non-disease state, both for download and dynamic, query-based exploration ("Tissues relating to AD").

Supplemental Information

Selective Neuronal Vulnerability

in Alzheimer's Disease:

A Network-Based Analysis

Jean-Pierre Roussarie, Vicky Yao, Patricia Rodriguez-Rodriguez, Rose Oughtred, Jennifer Rust, Zakary Plautz, Shirin Kasturia, Christian Albornoz, Wei Wang, Eric F. Schmidt, Ruth Dannenfelser, Alicja Tadych, Lars Brichta, Alona Barnea-Cramer, Nathaniel Heintz, Patrick R. Hof, Myriam Heiman, Kara Dolinski, Marc Flajolet, Olga G. Troyanskaya, and Paul Greengard

Supplemental Materials:

Supplemental Figure S1 to S4
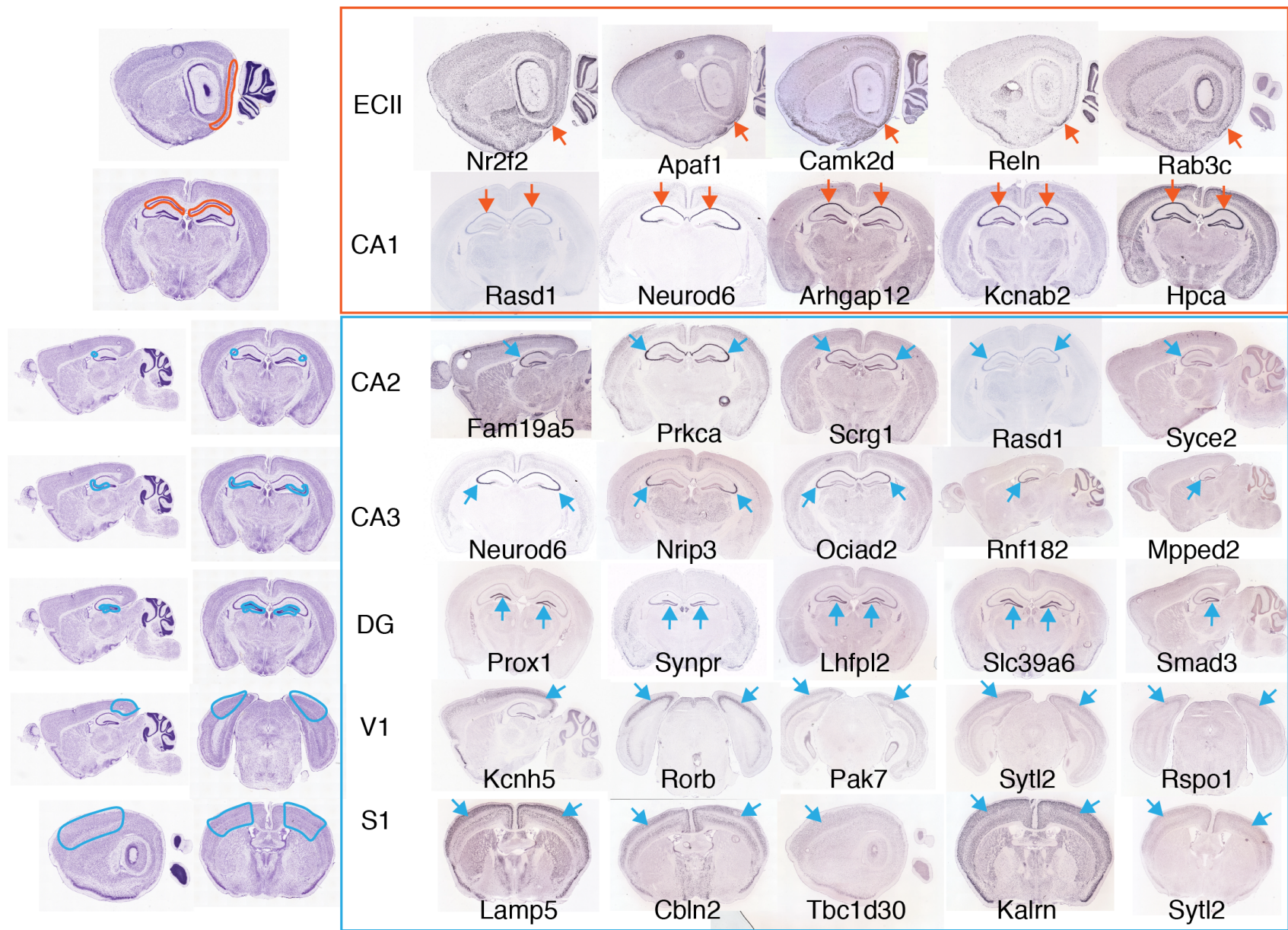
Supplemental Table S7

Figure S1: Validation, using the ABA, of the most enriched genes in each neuron type in the bacTRAP data. Related to Figure 2. For each neuron type, we examined the expression pattern of the genes with the top 50 z-scores of enrichment in the ABA. More than 85% of top genes showed expression in the correct region in the ABA (see Supplemental Note). We show here ISH data from ABA for the top 5 available genes for each region that have at least some expression in any part of the brain. We show sagittal sections for ECII neurons, and coronal sections whenever available or else sagittal sections for the other neuron types. The arrows point to the region of interest. Images of the reference atlas are shown on the left, with the region of interest outlined in orange (ECII and CA1) and blue (CA2, CA3, DG, V1, S1) Image credit: Allen Institute.
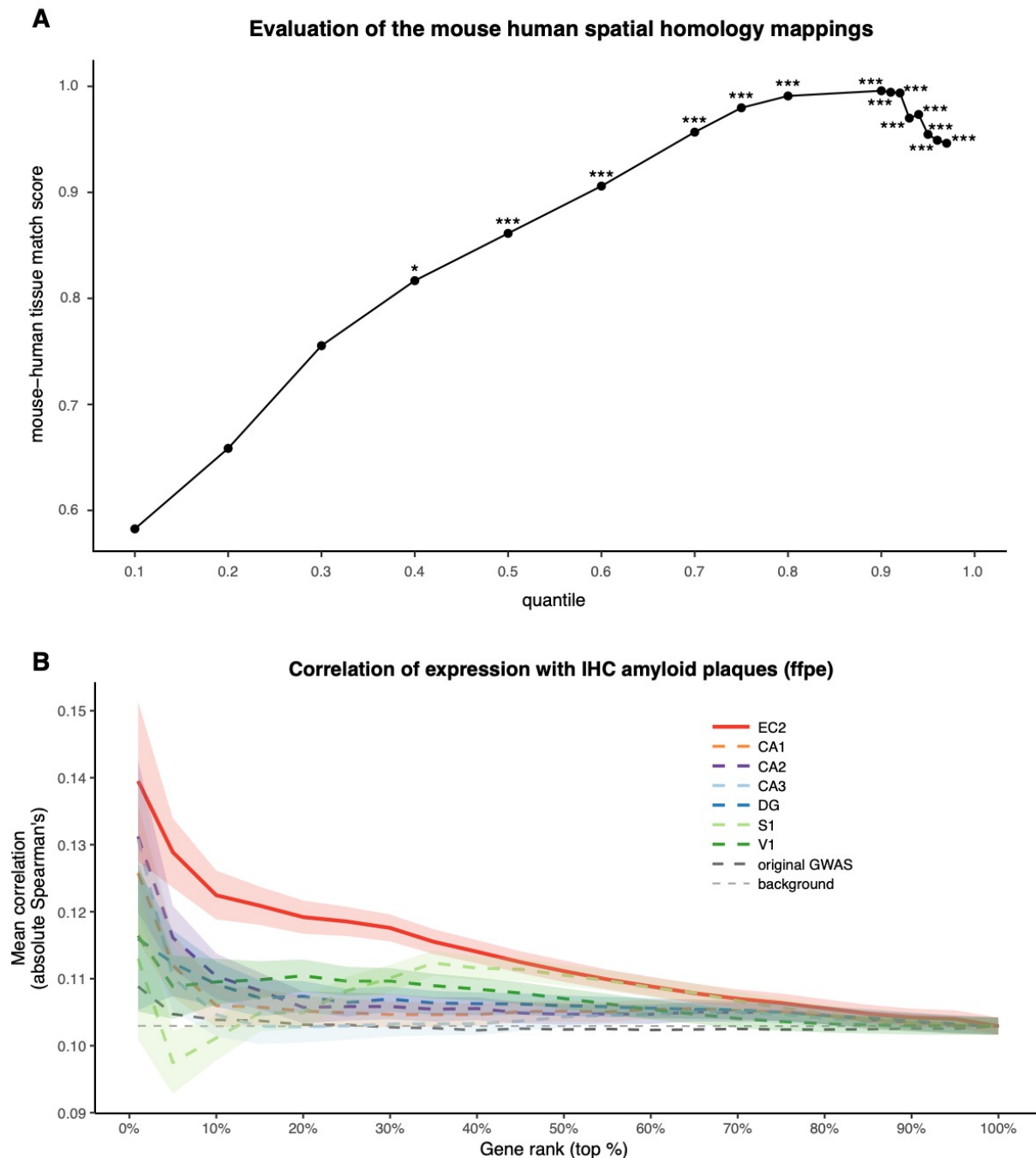
A

Evaluation of the mouse human spatial homology mappings

B

Correlation of expression with IHC amyloid plaques (ffpe)

Figure S2. A. Evaluation of the mouse-human spatial homology mappings. Related to Figure 3. Mouse-human tissue match score (1 = perfect match) at different quantile cutoffs (see Methods) improves with more specificity but decreases slightly as the molecular signatures have too few genes. Stars correspond to significance of score based on permutation tests (n=1000): (*: pval < 0.05, **: pval < 0.01, ***: pval < 0.001). **B. Correlation between amyloid plaque amounts and human hippocampal expression levels for NetWAS 2.0 gene predictions generated with functional networks specific of each neuron types. Related to Figure 4.** For most neuron types there was correlation between top NetWAS 2.0 and amyloid plaque amounts(Miller et al., 2017), but the correlation was much greater for ECII top predictions compared to top predictions for other neuron types. The x-axis represents the proportion of top NetWAS 2.0 genes obtained. The average absolute values of correlations between gene expression level and amyloid plaques across the subset of genes are plotted (NetWAS 2.0 predictions in color with 95% confidence interval - red for ECII, orange for CA1, purple for CA2, light blue for CA3, dark blue for DG, light green for S1, dark green for V1; Braak GWAS in black; background genes in grey).
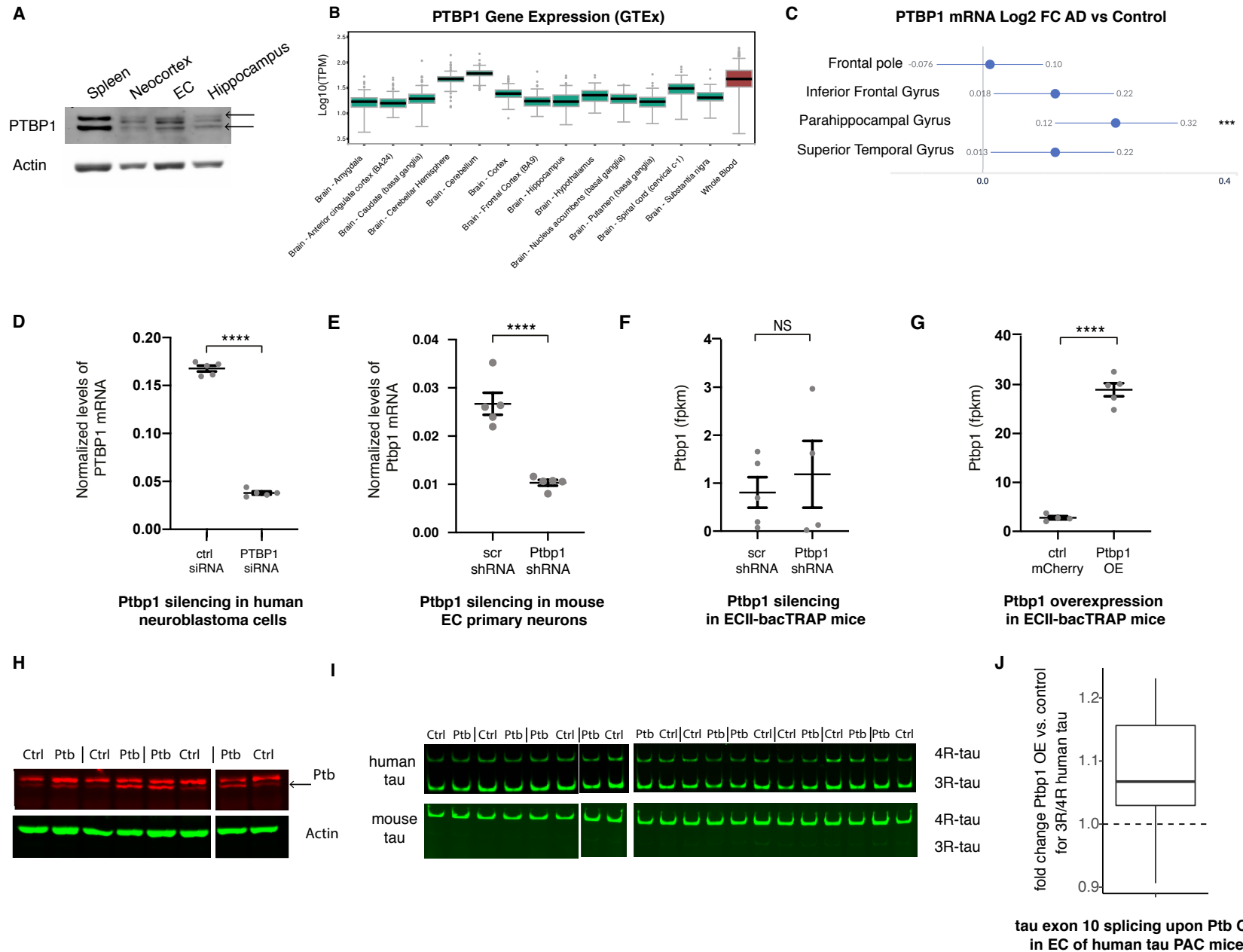
Figure S3. PTB is a modulator of human tau splicing. Related to Figure 5. A. Ptb is expressed in adult mouse brain. Lysates of spleen, neocortex, EC and hippocampus were probed by western blot in the adult mouse for Ptb expression. Although the spleen expressed higher levels of Ptb, there was also clear expression of Ptb in different brain regions (arrows show the two bands corresponding to Ptb. The band in between corresponds to Ptbp2). **B.** GTeX data also shows evidence for PTB expression across different adult brain regions. **C.** PTB mRNA is upregulated in AD vs. control patients specifically in the

parahippocampal region, where the EC is located (data from the Mount Sinai Brain Bank cohort obtained from the Agora portal), logFC = 0.22, adjusted p-value = 0.0004. **D.** Measurement of PTB mRNA in human neuroblastoma cells by qPCR, 72 hours after its siRNA silencing. Levels of PTB were decreased by 77 % (n = 5 independent wells, Student's *t*-test one-tailed p-value < 0.0001, error bars show standard error of the mean). (corresponding to Figure 5A, B, C). **E.** Evaluation of mouse Ptbp1 silencing in mouse EC primary cultures. We measured the levels of Ptb1 by qPCR, 96 hours after transduction with AAV1 particles carrying an shRNA against Ptb. Levels of Ptb were decreased by 61 % (n = 5 independent wells, Student's *t*-test one-tailed p-value < 0.0001, error bars show standard error of the mean). **F.** Evaluation of mouse Ptb silencing i*n vivo* in ECII neurons using the same AAV1 particles as in E. We performed bacTRAP followed by RNAseq, 2 weeks after stereotaxic injection of the same AAV1 particles as in E, carrying an shRNA against Ptb, in the EC of ECII-bacTRAP mice. We could not find any significant difference in the levels of Ptb in ECII neurons (n = 4 and 5 independent mice, error bars show standard error of the mean). **G.** Evaluation of mouse Ptb overexpression *in vivo* in ECII neurons. We performed bacTRAP followed by RNAseq, 2 weeks after stereotaxic injection of AAV1 particles carrying a Ptb cDNA (Ptb Δexon 9, NM_008956) in the EC of ECII-bacTRAP mice. Ptb mRNA was overexpressed 10.3-fold in ECII neurons (n = 4 and 5 independent mice, edgeR FDR = 4.5 x 10^{-95}, error bars show standard error of the mean). This same injection scheme was used to overexpress Ptbp1 in human tau PAC mice. **H.** western blot detection of Ptb in the EC *in vivo*. The two sides of the same brain are loaded next to one another. This experiment and the one shown in Figure 5D are quantified together in figure 5F. **I.** Fluorescent PCR assay to test differential usage of human tau exon 10 on reverse-transcribed RNA from EC lysates. 3R-tau and 4R-tau in the lysate yield amplicons of different lengths. The two sides of the same brain are loaded next to one another. This experiment and the one shown in Figure 5E are quantified together in figure 5G. **J.** qPCR assay to test differential usage of human tau exon 10 on reverse-transcribed RNA from EC lysates. Taqman probes are used that are specific to either 3R- or 4R-tau. Boxplot showing significantly higher ratio of 3R/4R human tau after Ptb OE.
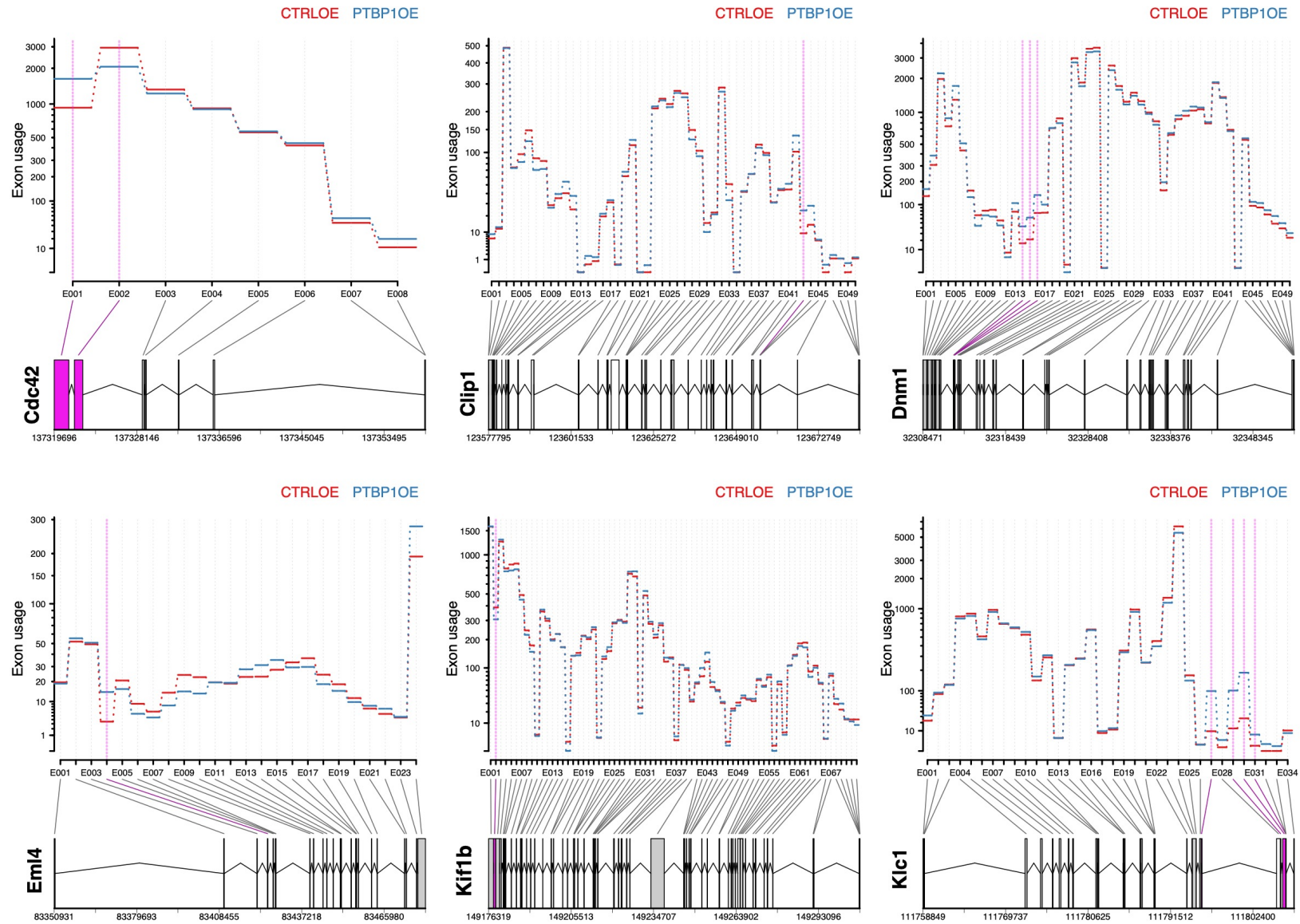
Figure S4. PTB modulates exon usage for various microtubule-associated genes (Cdc42, Clip1, Dnm1, Eml4, Kif1b, Klc1) in ECII neurons. Related to Figure 5. DEXSeq diagrams showing which exonic parts are differentially used in ECII neurons, two weeks after stereotaxic injections of PTB overexpression or control AAV (exonic parts in pink). ECII-bacTRAP mice were used for the injections, and mRNA was immunoprecipitated using the bacTRAP technique, ensuring specific profiling of ECII neurons (n = 4 and 5 independent mice per group).

Characteristics of the bacTRAP mice used for the profiling of specific neuron types				
Neuron type of interest	BacTRAP line	Number of replicates profiled	volume of lysis buffer used for the homogenization (in ml)	Small homology arm sequence
Principal neurons of entorhinal cortex layer II	Sh3bgrl2#26	5 replicates at 4-5 months, 3 replicates at 12 and 24 months	1	GCCTTTGCGTGTCTCTAAAACAGTGGGTCGCCTCAGCTCCATGGCTGTTTCTGATAGAGGATGCTCCACCCGTCTCCACCGCAAACAAAACCCAAGCTTGGACTATCCTCCACCCAACCCTTTGTCTTGTTTGCTGTGTTCTTGTAAACTGGCTTCCCGCCAATTAGCTTGTCCCGCTTCCGGGTCCTTCCTAAACCACCTGCGTGTACGATTAATTCCCGTGAAGCAGGCGCCGGACAGAAGGAGCGCAGTGCCTGGTCACTCTGGGCGCCAAGGAAACTACAACTCCCGTCAGCCCCCGCGGCCGCCTGGCCCCACCCGCCTCTCGCTCAGCCCGCGGCGGAGGCGCTGGGCTTTCATCCGCGGAGCGGCGGGAGCCAGACGCGTCGCTGCGGTCTTCTCCGACGGTCGCACGGGAGTCGGCAGCTACCTCAGTCGCGTTAAACTTCTGTGACCGAGTCAGCGGCGATCCCTGACGCAGCGA
	Sh3bgrl2#33	6 replicates at 4-5 months, 3 replicates at 12 and 24 months	1	GCCTTTGCGTGTCTCTAAAACAGTGGGTCGCCTCAGCTCCATGGCTGTTTCTGATAGAGGATGCTCCACCCGTCTCCACCGCAAACAAAACCCAAGCTTGGACTATCCTCCACCCAACCCTTTGTCTTGTTTGCTGTGTTCTTGTAAACTGGCTTCCCGCCAATTAGCTTGTCCCGCTTCCGGGTCCTTCCTAAACCACCTGCGTGTACGATTAATTCCCGTGAAGCAGGCGCCGGACAGAAGGAGCGCAGTGCCTGGTCACTCTGGGCGCCAAGGAAACTACAACTCCCGTCAGCCCCCGCGGCCGCCTGGCCCCACCCGCCTCTCGCTCAGCCCGCGGCGGAGGCGCTGGGCTTTCATCCGCGGAGCGGCGGGAGCCAGACGCGTCGCTGCGGTCTTCTCCGACGGTCGCACGGGAGTCGGCAGCTACCTCAGTCGCGTTAAACTTCTGTGACCGAGTCAGCGGCGATCCCTGACGCAGCGA
	199D5-Rasgrp2	3 replicates at 4-5 and 24 months, 2 replicates at 12 months	1.5	GCCCAGGAGGGGGAGATGTAGGCAGGACTCCTGGGTTCCCTCCTCCCTCCTTCCATCCCAGGGAGAAATTCCTCCGAGGTCCCCTCAGGCACTGGGTTCCCAAAATAACCCTGCGGGGGAAGGGAGGCTGTGAAGGGAGGGGAAGCGGGAGGGAGTGCAGAGTCAAGCTGTGGGGTGTTGCAGGTGCCTGTGGGGAGCAAATGCAAGGAGAGGAGGGGCCCGCCAGGAGGCTTGGGGCACTAACTAACCCCTGGGGTCCTGGCTCGTCCCTTATTCTCGTAGAACCCTTCTAACCTCCCGCGACTCCGCGGGTGGGCCGGAAGCCTCTCAGCTAGTCCATTTCCCAACTAGCGAGTTGCACCATCCCGGGGCAGGACCGTTTAACCCTAGAGGGGCAACGGCAGGCAACTCCGCCCATGCCCAGCAGGGGGCGTGCCCACTCCGCCCCGTTCCTACGCGCCGAGCCGCTCCCCCCACCTCCCGCGCCTCTGCTGACTCCCACTTCTCCCAGGACAGGGGTCCGAATTGAGCACCGTGGGAGGCTCTGAGAGTGTAGCTTGGGTCTAGCCTACTGGCACCGG
	344N1-Rasgrp2	3 replicates at each age	1.5	GCCCAGGAGGGGGAGATGTAGGCAGGACTCCTGGGTTCCCTCCTCCCTCCTTCCATCCCAGGGAGAAATTCCTCCGAGGTCCCCTCAGGCACTGGGTTCCCAAAATAACCCTGCGGGGGAAGGGAGGCTGTGAAGGGAGGGGAAGCGGGAGGGAGTGCAGAGTCAAGCTGTGGGGTGTTGCAGGTGCCTGTGGGGAGCAAATGCAAGGAGAGGAGGGGCCCGCCAGGAGGCTTGGGGCACTAACTAACCCCTGGGGTCCTGGCTCGTCCCTTATTCTCGTAGAACCCTTCTAACCTCCCGCGACTCCGCGGGTGGGCCGGAAGCCTCTCAGCTAGTCCATTTCCCAACTAGCGAGTTGCACCATCCCGGGGCAGGACCGTTTAACCCTAGAGGGGCAACGGCAGGCAACTCCGCCCATGCCCAGCAGGGGGCGTGCCCACTCCGCCCCGTTCCTACGCGCCGAGCCGCTCCCCCCACCTCCCGCGCCTCTGCTGACTCCCACTTCTCCCAGGACAGGGGTCCGAATTGAGCACCGTGGGAGGCTCTGAGAGTGTAGCTTGGGTCTAGCCTACTGGCACCGG
Pyramidal neurons of CA1	Sstr4#7	3 replicates at each age	1.5	GGGATGATGGCTCTGCGTGCTTGGGTGCTTGGGGTAATCTGGGGCCATCCAGATACTTTAATACCCAGAAAACTGTAGGTAGTGAGCGAGCGATTCGGAGAGAACCAGGATCCTAAGGGGAGAGGATCTGAAGAGCTGACGGAGGCGAGATCTAGCGGCACACGGTAGGACGGGTTCCAAGTAAAGTTTCTGATAGCCCGGCGAAACTGGCAACATGGCAGAGGTGGCGCAGGTAAGAAAAGCCCACAAGAGCTCTTCGGGCAAAGGCACCTGAGGTTGGGCGCGCGAAGGGAAGGGCGCGCCGGGCAAATGGAGCTCCCGCGGCCGAGGGGCGCGGCAGCGCAGGGATTGGCGGGTGCTCCCGGGCCCCCGCGCACTTCTTAGGCGGAGCGGCTGAGCCGAGCGTGTGCGCGCGCGACCCCAGCCCGCCTCTTGGTCCTTGGCTCAGCGCTCCGCTGCTCTCCACCGCATTCCGCTGCCCGGGGTGGGCACCCCGAGACATGAACGCGCCAGCAACTCTGCCTCCGGGGGTCGAGG
	Cck	6 replicates at 4-5 months, 3 replicates at 12 and 24 months	1	described in [23]
Pyramidal neurons of CA2	Cacng5	6 replicates at 4-5 months, 3 replicates at 12 and 24 months	1	GCCACCTCTGCTTAGATGTCAGCCAAGGCATGACATTGTCCCTAGGTAGGGTCCTGTGCCTGGTGGACTCAAAGTCGCTCAAACCATGGAAACCTTGGGGCAAGGTTCAACCCTTGCCCTTGTAACCCTAGGCTTACATCTTTTATAGAAGGTGGCGCTGTCCGCCCTTCTTCTGGGTTTAGGTCACTCTGAGCTTTCTCCACATATCAGTAACTTTTTCCATTTCTGTAACAAAATGCATAGCAAAAGCAACTTAAGGGAGAGTGTGTTAAGTCAATTAAATCTTTCCGAAAACATGTTTACAGCATACCCAGAGATGTGTTTCCACAGTGGCTCGAAATCTAATCAGGGTGGGTGGGTGGATGGATGGATGGATGGATGAATGGATGGATGGATGATGTGTAACTGGGTGGATAGGTGGATAGATGAATGGTCATGTATAGTAAGGGAAACTCAGAAGACAAGGGGATAGATACAGTAGCCTTAAGAGAAAGCTGTGAGTTCCTGAGGAGCATAGAGAGAGGGTCACCCTTAAGTGGAGATGGCCTGGACACTAGTAGCCTAGCTGCTCTTATTCACCCACTGACCCAGAGCAGACTGACTTCAGCTACTGCTCCCCACCTCCTGCTCACACTCTCTCTCTCTTCCCCACAGCCCATTCTGCACTCCTTGCTGCCCATCACCATCCA
Pyramidal neurons of CA3	Gprin3	3 replicates at each age	1	described in [76]

Granule neurons of Dentate Gyrus	Sstr4#19	3 replicates at each age	1.5	GGGATGATGGCTCTGCGTGCTTGGGTGCTTGGGGTAATCTGGGGCCATCCAGATACTTTAATACCCAGAAAACTGTAGGTAGTGAGCGAGCGATTCGGAGAGAACCAGGATCCTAAGGGGAGAGGATCTGAAGAGCTGACGGAGGCGAGATCTAGCGGCACACGGTAGGACGGGTTCCAAGTAAAGTTTCTGATAGCCCGGCGAAACTGGCAACATGGCAGAGGTGGCGCAGGTAAGAAAAGCCCACAAGAGCTCTTCGGGCAAAGGCACCTGAGGTTGGGCGCGCGAAGGGAAGGGCGCGCGCCGGGCAAATGGAGCTCCCGCGGCCGAGGGGCGCGCGGCAGCGCAGGGATTGGCGGGTGCTCCCGGGCCCCCGCGCACTTCTTAGGCGGAGCGGCTGAGCCGAGCGTGTGCGCGCGCGACCCCAGCCCGCCTCTTGGTCCTTGGCTCAGCGCTCCGCTGCTCTCCACCGCATTCCGCTGCCCGGGGTGGGCACCCCGAGACATGAACGCGCCAGCAACTCTGCCTCCGGGGGTCGAGG
Layer II/III and layer V neurons of S1	Cartpt	5 replicates at 4-5 months, 3 replicates at 12 and 24 months	3.5	GCCATCTGTCAGCCCATCAGAAAGGTTAACTTTGTGCTAAGGTACAGACTCTGGAAGTGATTGGCCCAGGACTGGTACCACGTCCGGTTCTCTCGCTCCCGTTCAGTTGAGTTACTCTACTTTCCTCTTCGGGTTATTAGTATCACACAGCCTCTACAGAGCCCTTGGTGCAGAGGACATAATTTCCCTTCGTCTAGTATGCTGATCATCTCCCTCACTCCCTAGCTTTCCTAGAATTGTGCTCAGCAAGTGAGCCTGCTGGAGTCCACATATCCTTCTTGCTGCTACACCCGGGGCTTGGGGATTAGGGAGGCAAAGCAGAGCCTATGAGCAGAACTCTGGTGCATCTACCACGGCTAAGATAGGGAAAACAACTCTTCTGCTTGTTCATTGCCCCGAAGGCATTTTCCATTTCCCTCACCTTTTGCCCCTCAGTTTCAGCTCTGGCCCCTAGGGAAGCTTCCCTGGCTGCGGGGCGGACAGCGTTTCGGGGCACGGGGTCTTGTTTTCTGCGCTCTAGCCCATCTGTGCGCAGAGCCTCGTTCCCGGGCTCCCGGAGCCCGGCGGGCATTGACGTCAAACGGCAGCGGAGCGCTGCCTACAGACGGCTGACCCGGGCTCTCCTCCACACCCCCGTCCTTCTTCTCCCCCTCCCTCTTCCCGGCACCCGATTTCAACCGGCTATAAGAAGCCGGAGAGCGCAGTGCCCGAGCAGCGAGGAGGTCCA
Layer IV neurons of V1	Calca	3 replicates at each age	3.5	GCCAATATGTAGCGAACAAGAGTCAGTTGCCGCAATTGCAAACCCCGATTTGGGACCCTGGGATTAACAGAGAAGTGTTTTCCACCTCAACTTTAGATTGGTTCTTGTAGGCAACTGAGTTGCCAGAGGGTGGAGCAGCTGAGCAGTGCAGCCGTCAGTTTCTCAGATTTCAAGGCAGAAAGATTCCCTCTCCATAGACTTTCTTTCTCACATTCTTAGGTGTCTGTAAAAAAACTCACAAAGAGAAGACAACTCTACACTTCCCTGTGGAGACAGATGTAGAGACAGGAGACACCTGGGATTCGTAGAATCCTTGAGACTGATCTCACCACCACCACTCCTTTACCACCACCACCACCACCACCACCACCACCCCCGACCCCCCGCACCCTCCCCCTCCTCCATCTTTAGGGCTAAGATTCTTTCCAAACCGTATAGGCTACATGCACACTGGACAATGAGGGAACAAAGATGATGAGAAATGTGGTTATCAGTATGAAGCCAAAATGTCGGGGAGTCACAGGCATAAGCACACAGAAAGCCAGGTCCATGGGCTTATAGAACCTTGAACTGATATAAATAAACAAATGAATAAATAGACATTCTTCTCTTGCAGGAAG

Genotyping primers		
Mouse type	primer name	primer sequence
all bacTRAP mice	GFP forward	5'-GACGTAAACGGCCACAAGTTCAG-3'
	GFP reverse	5'- ATGGTGCGCTCCTGGACGTAG-3'
APP/PS1 mice	APP forward	5'- AGGACTGACCACTCGACCAG-3'
	APP reverse	5'-CGGGGGTCTAGTTCTGCAT-3'
	PS1 forward	5'- AATAGAGAACGGCAGGAGCA-3'
	PS1 reverse	5'- GCCATGAGGGCACTAATCAT-3'
htau PAC mice	human tau forward	5'-ACTTTGAACCAGGATGGCTGAGCCC-3'
	human tau reverse	5'- CTGTGCATGGCTGTCCACTAACCTT-3'
	mouse tau forward	5'- CTCAGCATCCCACCTGTAAC-3'
	mouse tau reverse	5'-CCAGTTGTGTATGTCCACCC-3'

Table S7: characteristics of the bacTRAP mice used for the molecular profiling of seven different types of neurons, and sequence of primers used for mouse genotyping. Related to STAR methods.